# ENSO Asymmetry in CMIP5 Models

Tao Zhang and De-Zheng Sun

**Cooperative Institute for Research in Environmental Sciences**
**University of Colorado/NOAA Earth System Research Laboratory**
**Physical Sciences Division**
**Boulder, Colorado**

(*Submitted to Journal of Climate*)

December 19, 2013

Corresponding author address:
Dr. Tao Zhang
NOAA/ESRL/PSD
325 Broadway, R/PSD1
Boulder, CO 80305
Email: tao.zhang@noaa.gov

## Abstract

The El Niño–La Niña asymmetry is evaluated in fourteen CMIP5 coupled models. The results show that an underestimate of ENSO asymmetry, a common problem noted in CMIP3 models, remains a common problem in CMIP5 coupled models. The weaker ENSO asymmetry in the models primarily results from a weaker SST warm anomaly over the eastern Pacific and a westward shift of the center of the anomaly. In contrast, SST anomalies for the La Niña phase are close to observations.

Corresponding AMIP runs are analyzed to understand the causes of the underestimate of ENSO asymmetry in coupled models. The analysis reveals that during the warm phase, precipitation anomalies are weaker over the eastern Pacific and westerly wind anomalies are confined more to the west in most models. The time-mean zonal winds are stronger over the equatorial central and eastern Pacific for most models. Wind-forced ocean GCM experiments suggest that the stronger time-mean zonal winds and weaker asymmetry in the inter-annual anomalies of the zonal winds in AMIP models can both be a contributing factor to a weaker ENSO asymmetry in the corresponding coupled models, but the former appears to be a more fundamental factor, possibly through its impact on the mean state. The study suggests that the underestimate of ENSO asymmetry in the CMIP5 coupled models is at least in part of atmospheric origin.

## 1. Introduction

The El Niño–Southern Oscillation (ENSO)—a major source for interannual climate variability—affects weather and climate world-wide (Ropelewski and Halpert 1987; Kiladis and Diaz 1989; Hoerling et al. 1997; Larkin and Harrison 2005; Sun and Bryan 2010, Zhang et al. 2011, 2013). The two phases of ENSO—El Niño and La Niña—defined as tropical Pacific anomalies relative to a long-term average, are not mirror images of each other, but with the strongest El Niño being stronger than the strongest La Niña, a fact that has been referred as ENSO asymmetry (Burgers and Stephenson 1999).

The asymmetry between two phases of ENSO shows up in both the surface fields as well as in the subsurface fields (Rodgers et al. 2004; Schopf and Burgman 2006; Sun and Zhang 2006; Zhang et al. 2009). Causes for such an asymmetry are not yet clearly understood, but many studies suggest that it is likely a consequence of nonlinearity of the ocean dynamics (Jin et al. 2003; An and Jin 2004; Su et al. 2010). By the analysis of the heat budget of the ocean surface layer, Jin et al. (2003) and An and Jin (2004) found that the nonlinear vertical temperature advections are a major contributor to the ENSO amplitude asymmetry. However, based on the updated ocean assimilation products, Su et al. (2010) suggested that the nonlinear zonal and meridional ocean temperature advections are essential to cause the asymmetry in the far eastern Pacific, while the vertical nonlinear advection has the opposite effect. Another possible cause for the ENSO asymmetry is the asymmetric negative feedback due to the tropical ocean instability waves in the eastern Pacific that has a relatively stronger impact on the La Niña than El Niño (Vialard et al. 2001). Kang and Kug (2002) argued that the relatively weak SST anomalies during La Niña compared to those during El Niño result from the westward

73 shift of zonal wind stress anomalies during La Niña relative to El Niño. Such an
74 asymmetry in the zonal wind stress between two phases of ENSO is in turn attributed to
75 the nonlinear dependence of deep convection on the SST (Hoerling et al. 1997). A recent
76 review paper by An (2009) provides a good account of the aforementioned theories for
77 ENSO asymmetry. In a more recent study by Liang et al. (2012) using an analytical
78 model of Sun (1997), it is noted that ENSO asymmetry may depend on the radiative
79 forcing as in that model a stronger radiative forcing produces a stronger and more
80 positively skewed oscillation. They also attribute the asymmetry of the two phases of
81 ENSO—as traditionally defined as the deviations from the climatological mean—to the
82 asymmetry of the dynamics relative to the equilibrium state of the system.
83 Understanding the causes and consequences of ENSO asymmetry may hold the key to
84 understand decadal variability in the tropics and beyond, as the asymmetry suggests a
85 time-mean effect of ENSO (Rodgers et al. 2004; Schopf and Burgman 2006). Indeed, in
86 theoretical studies and numerical experiments designed to determine the time-mean effect
87 of ENSO, an association between the time-mean effect of ENSO and the asymmetry of
88 ENSO is found (Sun and Zhang 2006; Sun and Yu 2009; Sun et al. 2013; Sun et al. 2014),
89 although it appears that they are both a consequence of the nonlinearity. In order to fully
90 capture the role of ENSO in the climate system, the climate models need to simulate well
91 the asymmetry of ENSO.
92 The ENSO asymmetry in coupled models has been extensively examined in previous
93 studies (Burgers and Stephenson 1999; Hannachi et al. 2003; An et al. 2005; van
94 Oldenborgh et al. 2005; Zhang et al. 2009; Sun et al. 2013). The studies of Oldenborgh et
95 al. (2005) and Sun et al. (2013) made use of the archive of the CMIP3 models and found

96 that an underestimate of the asymmetry is a prevalent problem, capping the early findings
97 from a rather scattered set of models. However, the cause for the bias in ENSO
98 asymmetry is not well understood in those studies. In the complex coupled system it is
99 difficult to identify causes for biases in ENSO asymmetry owing to the strong feedbacks
100 of the ocean-atmosphere system in the tropical Pacific. Understanding the bias in coupled
101 models therefore requires the use of component models, such as stand-alone atmospheric
102 models, through which we can isolate the sources and amplifiers of biases in climate
103 models.
104
105 In the present study, we evaluate the ENSO asymmetry in CMIP5 models (Taylor et al.
106 2012). We follow the methodology of Zhang et al. (2009) and analyze the corresponding
107 AMIP runs as well in order to gain more insight into the possible causes of the bias in
108 ENSO asymmetry. By analyzing previous NCAR coupled models (CCSM1, CCSM2,
109 CCSM3 at T42, CCSM3 at T85, and CCSM3+NR) in conjunction with the corresponding
110 Atmospheric Model Intercomparison Project (AMIP) runs, Zhang et al. (2009) showed
111 that all the models underestimate the observed ENSO asymmetry, but CCSM3+NR with
112 Neale and Richter convection scheme (Neale et al. 2008) has significant improvements
113 over the earlier versions with Zhang and McFarlane convection scheme (Zhang and
114 McFarlane 1995). Enhanced convection over the eastern Pacific during the warm phase
115 of ENSO appears to be the cause for the improvement. Zhang et al. (2009) also noted a
116 warmer SST climatology in CCSM3+NR in contrast to other versions. We will explore
117 whether the underestimate of ENSO asymmetry remains a common problem in the state-
118 of-art coupled model; whether the underestimate of ENSO asymmetry in CMIP5 models

119 is related to the weaker convection over the eastern Pacific during warm phase; and
120 whether the mean SST state is important to ENSO asymmetry.
121
122 This paper is organized as follows. We introduce the observational and model data
123 sets in section 2. We present the analysis of ENSO asymmetry in CMIP5 models in the
124 coupled runs, and then the asymmetry in the corresponding AMIP runs. To understand
125 the impact of the biases identified from the analysis of the AMIP runs, the numerical
126 experiments forced by AMIP winds are conducted in section 3. Conclusions and
127 discussions are presented in Section 4.
128

129 **2. Data and Methods**

130 The ENSO asymmetry in fourteen coupled ocean-atmosphere models from CMIP5
131 control runs (piControl) has been evaluated in this investigation. Presented here are the
132 results from the coupled models whose corresponding AMIP runs are available for the
133 analysis. We will first assess the ENSO asymmetry in the SST and then look at the
134 asymmetry in upper ocean temperature in the models. We further analyze the
135 corresponding fields of precipitation and surface wind stress in the coupled runs to
136 understand whether the bias in ENSO asymmetry is linked to the bias in precipitation and
137 associated surface wind stress. The corresponding AMIP runs from CMIP5 models are
138 also examined to understand whether the biases in precipitation and surface wind stress in
139 coupled runs stem from the biases in stand-alone atmosphere models.
140 In addition to analyzing the asymmetry in the CMIP5 AMIP runs, we also use the
141 NCAR Pacific basin model to perform the forced ocean experiments driven by CMIP5

142 AMIP winds. Our model is the one used by Sun (2003), Sun et al. (2004) and Sun and
143 Zhang (2006). The model uses the NCAR Pacific basin model (Gent and Cane, 1989) as
144 its ocean component. The model calculates the upper ocean temperatures based on first
145 principles and simulates well the observed characteristics of ENSO in both the forced and
146 coupled modes (Sun 2003). We will compare the ENSO asymmetry in the runs forced by
147 AMIP winds with that by observed winds to understand the effect of the bias in the
148 atmospheric response on ENSO asymmetry in CMIP5 coupled models.

149 The observational data used for examining the model results are the same as those
150 used by Zhang et al. (2009). The SST data from the Hadley Centre Sea Ice and SST
151 (HadISST) dataset (Rayner et al. 2003) are used for evaluating the asymmetry in the SST
152 field in the CMIP5 coupled models. The simple ocean data assimilation (SODA) set
153 (Carton et al. 2000) is used for validating the upper-ocean temperature in the models.
154 Precipitation data are obtained from the Climate Prediction Center (CPC) Merged
155 Analysis of Precipitation (CMAP; Xie and Arkin 1997). The wind stress data are
156 obtained from the simple ocean data assimilation (SODA) set (Carton and Giese 2008) in
157 which the surface winds are a combination of ERA-40 and Quick Scatterometer
158 (QuikSCAT) satellite observations.

159 We will use the skewness (Burgers and Stephenson 1999) of interannual variability of
160 SST to quantify the ENSO asymmetry. We will also conduct the composites of El Niño
161 and La Niña and then use the sum of the composite between two phases of ENSO to
162 measure the asymmetry. The definition of the warm phase and cold phase of ENSO
163 follows that of Zhang et al. (2009). The composite analysis will help to identify which
164 phase of ENSO the bias in ENSO asymmetry mainly originates from.

## 3. Results

### *a. Asymmetry in the coupled models*

A quantitative measure of the ENSO asymmetry in CMIP5 coupled models reveals that an underestimate of the ENSO asymmetry remains a common bias in our state-of-the-art climate models. Figure 1 shows the skewness of Niño-3 SST anomalies from observations and the models, together with their variance. Measured by the variance of Niño-3 SST, ENSO in many models is as strong as in observations. But measured by the skewness of Niño-3 SST, all the coupled models that we have analyzed underestimate the observed positive ENSO asymmetry. This indicates that the observed SST anomalies in the eastern Pacific are skewed toward warm events, while those in coupled models have a more Gaussian-like distribution. In comparison, the NCAR CCSM4 model (Gent et al. 2011; Deser et al. 2012) stands out as the best model in simulating the ENSO asymmetry, whose variability of ENSO is also comparable to observations. The HadGEM2-ES model, which also has a comparable ENSO variability to observations, is found to have the largest bias in reproducing the observed positive skewness, because it shows a strong negative skewness, contrary to observations. The results suggest that the stronger variability of ENSO (measured by variance) does not guarantee a stronger asymmetry (measured by skewness) in CMIP5 coupled models.

Figure 2 shows the sum of the SST anomalies between the warm and cold phases of ENSO from observations and coupled runs from CMIP5. This sum has also been called SST anomaly residual and is a common measure of the ENSO asymmetry in the SST field. The SST anomaly residual results are similar to the skewness map of SST

188 anomalies (not shown). All the CMIP5 models evaluated underestimate the observed
189 positive SST residual and, therefore, the asymmetry over the eastern Pacific, consistent
190 with the results of skewness. There is an obvious negative SST residual over the eastern
191 Pacific in HadGEM2-ES model, in agreement with a considerable negative skewness of
192 Niño-3 SST anomalies in this model (Figure 1). Generally, CCSM4 model has a better
193 simulation of the positive SST residual in the eastern Pacific than other models, which is
194 also confirmed by the skewness results noted earlier. Despite the fact that all the models
195 underestimate the positive SST residual over the eastern Pacific, the overestimate of the
196 negative SST residual in the western Pacific is evident in many models (e.g. GISS-E2-R,
197 MIROC5, CSIRO-MK3-6-0, CCSM4).

198 As already noted in the analysis of the previous NCAR models and consistent with
199 earlier understanding of ENSO dynamics, the asymmetry in the subsurface temperature is
200 more profound than in the surface (Zhang et al. 2009). To obtain more information about
201 the cause for the bias in simulated ENSO asymmetry, we look at the asymmetry of the
202 subsurface signal. Figure 3 shows the sum of the equatorial upper-ocean temperature
203 anomalies between the warm and cold phases of ENSO from observations and coupled
204 runs from CMIP5 models. The observed subsurface temperature shows a positive
205 asymmetry of about 1°C around 75-m depth over the eastern Pacific and a negative
206 asymmetry of about -0.4°C around 150-m depth over the western Pacific. All the models
207 underestimate the positive asymmetry in the subsurface temperature over the eastern
208 Pacific. In contrast to the asymmetry in SST, the underestimate of the positive asymmetry
209 in the subsurface temperature is more profound over the eastern Pacific (note the
210 different scale in Figure 2 and Figure 3). Most models also have a weaker negative

asymmetry in the subsurface over the western Pacific. Despite the comparable magnitude to observations, the negative asymmetry over the western Pacific extends too far to the east in some models (CNRM-CM5, FGOALS-g2, CCSM4). There is a good match between SST and subsurface temperature for the negative asymmetry in HadGEM2-ES over the eastern Pacific (Figure 3 and Figure 2). Consistent with the stronger positive SST residual over the eastern Pacific, CCSM4 also has a stronger positive residual in the subsurface. Again, the bias in SST asymmetry appears to be linked to the bias in the asymmetry of the subsurface temperature, as noted in Zhang et al. (2009).

To explore which phase of ENSO is the major source for the weaker residual in the SST and the subsurface in CMIP5 models, we investigate the spatial distribution of composite anomalies during two phases of ENSO. Figure 4 gives the spatial pattern of composite SST anomalies during the warm phase of ENSO. Observations show that the stronger positive SST anomalies associated with warm events are located over the South American coast and the maximum value can reach about 1.6°C. Most models have a weaker SST warm anomaly over the eastern Pacific, and the underestimate of the warm SST anomaly is more serious in the coastal regions (100°W-80°W). The simulated maximum center is found to shift westward in many models. These biases contribute to the weak SST residual in the models (Figure 2). The observed maximum center around 110°W is well captured in CCSM4 model that has an enhanced warm anomaly over the coastal regions which contributes to the increase in SST residual (Figure 2).

The bias in the warm anomalies also shows up in the subsurface (Figure 5). Consistent with the bias in the SST warm anomalies, most models have a weaker subsurface warm anomaly over the eastern Pacific and the simulated maximum center is

234 shifted westward. The better simulation of SST warm anomalies in CCSM4 model is
235 apparently associated with the improvement in the simulation of warm anomalies of
236 subsurface temperature. Over the western Pacific, the underestimate of the negative
237 anomalies in the subsurface is also evident in many models. The negative anomalies in
238 the subsurface over the western Pacific in NorESM1-M model are much stronger and
239 extend too far to the east during the warm phase, causing a more stronger and eastward
240 extended negative asymmetry in this model (Figure 3).

241 To better understand the cause for the underestimate of the ENSO asymmetry in
242 CMIP5 coupled models, the spatial map of the difference between models and
243 observations for the composite SST anomalies during two phases of ENSO as well as
244 time mean SST is displayed in Figure 6. Clearly, the underestimate of the warm
245 anomalies is the major cause for the weaker ENSO asymmetry in CMIP5 coupled models,
246 and the contribution from the bias during the cold phase of ENSO is small. We also note
247 that CMIP5 models have a strong cold bias in mean SST state, a prevalent problem in
248 coupled models (Sun et al. 2006; Zhang et al. 2009), which implies a possible link
249 between the bias in mean SST state and the bias in ENSO asymmetry.

250 Figure 7 further shows the sum between the warm composite anomalies and cold
251 composite anomalies in precipitation (shaded) and zonal wind stress (contours) from
252 observations and coupled models. The observed precipitation is characterized by a strong
253 positive asymmetry in the central and eastern Pacific and a strong negative asymmetry in
254 the western Pacific, resulting from the westward shift during the cold phase compared to
255 the warm phase (Zhang et al. 2009). The underestimate of the positive precipitation
256 asymmetry over the central and eastern Pacific is prominent in the models. Consistent

257 with the weak asymmetry in the precipitation, the asymmetry in zonal wind stress is also
258 weak in the coupled models, which is expected from the weak asymmetry in the
259 subsurface temperature noted earlier.

260 *b. Asymmetry in the AMIP runs*

261 To understand whether the weaker asymmetry in precipitation and wind stress in
262 CMIP5 coupled models is a consequence of the corresponding SST fields or the cause of
263 the latter, we perform the composite analysis from the corresponding AMIP runs of
264 CMIP5 models that are forced by the observed SST boundary conditions. The AMIP runs
265 involve subjecting the atmospheric component of CMIP5 coupled models to the observed
266 ENSO SST variability and thus specifying the full ENSO asymmetry. The specification
267 of the observed ENSO conditions in the AGCMs greatly increases the asymmetry in
268 tropical Pacific rainfall, especially over the central Pacific where the AMIP results are in
269 much better agreement with observations than the results from coupled runs (Figure 8).
270 However, many models have a weaker precipitation asymmetry over the eastern Pacific.
271 The NCAR model, which has proved to be the best model in simulating the ENSO
272 asymmetry, is found to have a comparable precipitation asymmetry in the eastern Pacific.
273 This suggests that the realistic simulation of precipitation asymmetry in the eastern
274 Pacific may be an important factor for a better simulation of ENSO asymmetry.

275 Figure 9 shows a quantitative measure of the precipitation asymmetry over the eastern
276 Pacific. The top panel is results from the coupled runs and the bottom panel is those from
277 the corresponding AMIP runs. All the coupled models have a weaker precipitation
278 asymmetry over the eastern Pacific. By comparison, the CCSM4 coupled model has the
279 largest value of precipitation asymmetry. The increase in precipitation asymmetry from

coupled runs to AMIP runs is also evident over the eastern Pacific. We also note that nine of fourteen AMIP models have a weaker precipitation asymmetry over the eastern Pacific even driven by the observed SST forcing. Two AMIP models (NorESM1-M and MRI-CGCM3) have a comparable precipitation asymmetry to the observed and the other three AMIP models (GISS-E2-R, CCSM4, and bcc-csm1-1) have a slightly larger precipitation asymmetry. The error of the weaker asymmetry in precipitation is apparently amplified in coupled runs as the coupled runs are found to have a much weaker precipitation asymmetry than their corresponding AMIP runs. There is a significant positive correlation (0.58) for the precipitation asymmetry averaged over the eastern Pacific between fourteen AMIP runs and coupled runs. The weak precipitation asymmetry over the eastern Pacific is mainly due to the bias in the warm phase (Figure 10). Nine of fourteen AMIP models have a weaker precipitation warm anomaly over the eastern Pacific. The precipitation warm anomaly is well captured in three models (HadGEM2-ES, MRI-CGCM3, and bcc-csm1-1) and somewhat overestimated in the other two models (GISS-E2-R, and CCSM4). Again, the corresponding coupled models have a much weaker precipitation warm anomaly and all the coupled models underestimate the observed precipitation warm anomaly. This seems to indicate that the insufficient precipitation response to El Niño warming over the eastern Pacific is an intrinsic error of the majority of the atmospheric models. Further studies are needed to understand the cause of the bias in precipitation by exploring whether the model simply does not respond to the SST anomalies correctly in a local sense or there is a non-local influence from surface zonal stress, convergence and the local reversal of the Walker circulation allowing or suppressing the ascent in the eastern Pacific.

303 Figure 11 further shows the spatial pattern during the warm phase for observations,
304 the ensemble mean AMIP runs, and the differences between them. The left panel shows
305 the precipitation and the right one the zonal wind stress. Consistent with the results
306 shown in Figure 10 bottom, there is a weaker precipitation response over the eastern
307 Pacific in the AMIP runs. Note that the precipitation warm anomalies in the AMIP runs
308 are somewhat stronger over the central Pacific, and this positive bias is also reflected in
309 the precipitation residual (Figure 8), further confirming that the bias in the warm phase of
310 ENSO is the major source for the bias in ENSO asymmetry. In contrast to observations,
311 the precipitation response shows a less eastward extension (indicated by shaded values)
312 in the AMIP runs during the warm phase. Linked to the precipitation response, the
313 westerly wind (positive) anomaly is positioned too far to the west and shifts westward by
314 about $10^{o}$ (indicated by green lines shown on Figure 11 right panel, top two). Similar to
315 the precipitation difference, there is an obvious negative (weaker westerly wind) anomaly
316 over the eastern Pacific and a positive (stronger westerly wind) anomaly over the central
317 Pacific (Figure 11 right panel, bottom). The westward shift of the zonal wind stress warm
318 anomalies in the AMIP runs may contribute to the weaker warm anomaly of subsurface
319 temperature in most coupled models during the warm phase (Kang and Kug 2002). In
320 addition to the westward shift of westerly wind anomaly, the significant easterly wind
321 anomaly in the far eastern Pacific may also be responsible for the bias in subsurface
322 temperature by inducing anomalous upwelling.
323 The CMIP5 AMIP runs are found to have biases in the mean zonal winds over the
324 equatorial central and eastern Pacific and in the asymmetry in the central Pacific wind
325 variability (Figure 12). Eleven of fourteen models have a stronger mean zonal wind in

AMIP runs, and the other three models (HadGEM2-ES, CCSM4 and CSIRO-MK3-6-0) have a comparable mean wind to the observed. Ten of fourteen models underestimate the observed positive skewness of central Pacific zonal winds in AMIP runs. Models CNRM-CM5 and bcc-csm1-1 have a better simulation of the observed wind skewness, while models IPSL-CM5A-LR and MPI-ESM-LR have a stronger skewness in the zonal wind stress and the mean winds are also much stronger in these two models, especially in the latter. Generally, the ensemble mean results show that the AMIP runs have a stronger mean winds and a weaker skewness in the zonal winds.

The spatial map of time mean zonal wind stress shows that there is a stronger mean wind in the models over most regions of the equatorial Pacific (Figure 13). The bias in the mean wind (negative values) is more significant in the coastal regions (110$^{o}$W-90$^{o}$W, 0-10$^{o}$N), where the mean precipitation is also much underestimated in the AMIP run. The stronger tropical winds are accompanied with excessive precipitation over much of the tropics, especially over the regions off the equator. More specifically, the mean precipitation difference is characterized with generally negative bias within the ITCZ (intertropical convergence zone) and with positive bias elsewhere. The similar biases in winds and precipitation were also found in the previous CMIP3 AMIP runs (Lin 2007). There is a clear east-west asymmetry in the precipitation bias and the resulting excessive zonal latent heating gradient associated with zonal precipitation gradient may drive the stronger winds in the model (Lin 2007). The results indicate that the climatological wind is an important cause of ENSO asymmetry. Specifically, the stronger mean winds will lead to a colder mean SST state that may suppress the increase of SST anomaly during the warm phase of ENSO, but has less effect on the SST anomaly during the cold phase

of ENSO. Probably associated with the dependence of the oceanic response on the mean SST state (McPhaden et al. 2011; Chung and Li 2013), this nonlinear effect of a colder mean state on the SST anomaly during the two phases of ENSO may be responsible for a weaker ENSO asymmetry. The biases in the surface winds from AMIP runs play a role in the ENSO asymmetry, which will be shown by the following numerical experiments.

### *c. Numerical experiments*

To understand the biases of model winds associated with convection in AMIP runs on the ENSO asymmetry in CMIP5 coupled models, we use the NCAR Pacific basin model (Sun 2003; Sun et al. 2004; Sun and Zhang 2006) to perform numerical experiments. We conduct the forced ocean model experiments with the use of ensemble mean AMIP winds from fourteen CMIP5 models and compare the results with those from the forced ocean runs driven by the observed wind stress. Four groups of numerical experiments combined with different climatology and interannual anomalies of winds in observations and ensemble mean AMIP runs of CMIP5 models are listed in Table 1. We first perform the forced ocean experiments with both climatology winds and interannual anomalies of winds from observations (Experiment I). To understand the role of climatology winds in the models, we then replace the observed climatology winds by the modeled climatology winds but keep the observed interannual anomalies of winds unchanged in the forced experiments (Experiment II). Next, we use the actual AMIP model winds that include the simulated climatology and interannual anomalies to drive the ocean model, which will further explore the role of modeled interannual anomalies in the surface winds on ENSO asymmetry (Experiment III). Finally, to explore the role of observed climatology winds, we replace the modeled climatology winds with the observed climatology winds but keep

372 the modeled interannual anomalies of winds to drive the ocean (Experiment IV). These
373 experiments are designed to probe the relative role of the bias in climatology winds and
374 interannual variability of winds in AMIP runs in causing the underestimate of ENSO
375 asymmetry in CMIP5 coupled runs.

376 Table 1 shows the standard deviation and skewness of the interannual variability in
377 Niño-3 SST from four forced ocean runs. Driven by observed winds (Experiment I), the
378 model can well reproduce the observed skewness value of Niño-3 SST anomalies. The
379 skewness value of 1.16 in Experiment I is very close to the observed skewness value of
380 1.05 over the same 30-year period. The results in the table show that the skewness from
381 the run forced by full model winds (0.70 in Experiment III) is about 40% weaker than
382 that from the run by the observed winds (1.16 in Experiment I) accompanied by a
383 weakened variability. By comparing the results from two cases that use the same
384 observed wind anomaly but different wind climatology (Experiment I and Experiment II),
385 we find the bias in the modeled wind climatology is partially (~50%) responsible for the
386 reduction in the ENSO asymmetry. The use of simulated wind interannual anomalies will
387 further reduce the ENSO asymmetry, as the skewness in the run with full model winds is
388 the smallest (Experiment III). Interestingly, we note that the skewness in the case with
389 observed wind climatology but keeping simulated wind interannual anomalies
390 (Experiment IV) is comparable to that in the run by the observed full winds (Experiment
391 I), although the variability remains weak. The results from Experiments III and IV
392 indicate that the improvement in mean winds play a dominant role in improving the
393 simulation of ENSO asymmetry.

394 The residual pattern of SST shows that there is a progressive decrease in the positive
395 SST residual over the Niño-3 region from Experiment I to Experiment III (Figure 14)
396 consistent with the skewness value shown in Table 1. The decrease in the positive SST
397 residual is more obvious in Experiment III when full model winds are used. There is also
398 a gradual westward shift in the positive SST residual, and the westward shift is also
399 visible in the subsurface. The positive SST residual over the Niño-3 region is greatly
400 increased from Experiment III to Experiment IV when observed mean winds are used to
401 replace the modeled mean winds, although there is a lack of evident positive SST residual
402 over the coast regions (100°W-80°W) in these two cases. Thus compared to observed
403 wind anomalies, the wind anomalies in models can reduce the positive SST residual over
404 the coast regions.
405 Figure 15 shows the spatial map of the composite anomalies of SST (left panel) and
406 the equatorial upper ocean temperature (right panel) during the warm phase of ENSO
407 from four forced ocean experiments. The NCAR Pacific basin model used in this study
408 reproduces the pattern of observed SST warm anomalies (Figure 4). The simulated
409 stronger SST warm anomalies in the run forced by observed winds (top left) are located
410 over the South American coast. The bias in the modeled wind climatology causes a slight
411 westward shift of stronger SST warm anomaly but does not reduce the magnitude
412 (second row left). Accompanied with a weaker subsurface temperature warm anomaly
413 (third row right), the westward shift of SST warm anomaly is more evident and the
414 magnitude of SST warm anomaly becomes weaker if the bias in the interannual anomaly
415 of modeled winds is also involved (third row left). The features of SST and subsurface
416 temperature warm anomalies in the run forced by full model winds also exist in CMIP5

417 coupled models (Figure 4 and Figure 5). The comparison between Experiments III and IV
418 shows that changing mean winds from models to observations alone can increase SST
419 warm anomalies. Due to the use of the same model wind anomalies, the westward shift of
420 SST warm anomaly is still evident in Experiment IV. This is consistent with the lack of
421 positive SST residual over the coast regions noted earlier (Figure 14).

422 During the cold phase of ENSO (Figure 16), bias in the modeled wind climatology
423 somewhat increases the magnitude of cold SST anomalies over the Niño-3 region and
424 thus reduces the SST skewness. The increase in cold SST anomaly magnitude is linked to
425 the stronger cold subsurface temperature (second row). Interestingly, the inclusion of
426 wind anomalies from models is found to significantly reduce the magnitude of SST warm
427 anomalies, but does not deteriorate the bias in cold SST anomalies (third row). Instead,
428 the cold SST anomalies and subsurface temperature anomalies are comparable to those in
429 the run forced by observed full winds. This also supports the previous analysis that the
430 underestimate of the SST skewness in CMIP5 models is mostly due to bias in the warm
431 phase. The Experiment IV results show that the observed mean winds can reduce the cold
432 SST anomalies, favoring an increase of SST skewness. Among the four runs, Experiment
433 IV has a more confined cold SST anomaly within the equatorial Pacific, while the other
434 three runs show a more meridional extension of the cold SST anomalies, especially over
435 the southern equatorial Pacific. The weakened cold SST anomalies over the Niño-3
436 region in Experiment IV is linked to the reduction in cold subsurface temperature
437 anomalies.

438 Figure 17 shows the time-mean SST difference and the equatorial upper ocean
439 temperature difference of Experiments II, III, IV from Experiment I. Compared to

Experiment I, there is a stronger cold SST over the cold-tongue regions in Experiments II and III, in which the observed mean winds are replaced with mean winds from models. The subsurface temperature is also colder in these two cases that have a weaker SST skewness. By comparison, the SST and subsurface temperature in Experiment IV are comparable to those in Experiment I, since these cases use the same observed mean winds.

Note that different from Experiment I, Experiment IV uses the interannual anomalies of winds from models but still has a comparable SST skewness to the observed. This suggests that the mean SST state induced by mean winds is fundamentally important to the simulation of ENSO asymmetry, and the bias in wind variability is secondary.

In general, the effect of the bias in interannual anomalies of modeled winds on ENSO asymmetry is mainly attributed to wind bias in the warm phase—a westward shift of the zonal wind stress warm anomalies in the AMIP runs, linked to the insufficient precipitation response over the eastern Pacific during the warm phase (Figure 11). These numerical experiments demonstrate that when there is a colder mean SST state due to the stronger mean winds in models, the biases in interannual anomalies of winds from AMIP runs can weaken ENSO asymmetry by shifting SST warm anomalies westward and reducing their magnitude. When there is a warmer mean SST state, or the model mean winds are the same as observations, the ENSO asymmetry can be as large as that in the run with observed full winds, and the contribution to ENSO asymmetry from the bias in wind interannual variability is small.

## 4. Summary

463 In this study, we have evaluated the accuracy of CMIP5 coupled models in simulating
464 the ENSO asymmetry and explored causes for bias in ENSO asymmetry in CMIP5
465 coupled models by analyzing the corresponding AMIP runs of CMIP5 coupled models
466 and by conducting forced ocean GCM experiments with the winds from CMIP5 AMIP
467 runs.

468 Previous analysis of CMIP3 coupled models noted that, different from observations,
469 most coupled models have a near zero SST skewness in the tropical Pacific and a linear
470 ENSO (van Oldenborgh et al. 2005; Sun et al. 2013). The present findings show that the
471 underestimate of observed positive ENSO asymmetry measured by skewness is still a
472 common problem in CMIP5 coupled models, although many models have comparable
473 variance in Niño-3 SST with respect to observations—a significant improvement over
474 CMIP3. When the asymmetry is measured by the SST residual between the two phases of
475 ENSO, all the models are also found to have a weaker ENSO asymmetry than
476 observations. It is notable that CMIP5 coupled models have a significant cold bias in the
477 mean SST as seen in many coupled models (Sun et al. 2006; Zhang et al. 2009). The
478 weak ENSO asymmetry in CMIP5 models has corresponding signatures in biases in
479 zonal wind stress, precipitation and subsurface temperatures, which are also too
480 symmetrical with respect to ENSO phases. The composite analysis indicates that the
481 weaker asymmetry of ENSO in CMIP5 coupled models is largely a consequence of the
482 bias from El Nino events. The SST warm anomalies over the far eastern Pacific are found
483 to be weaker in the coupled models than in observations and the simulated maximum
484 warm SST center over the eastern Pacific shifts westward. Most models also have a
485 weaker subsurface temperature warm anomaly over the eastern Pacific and the maximum

center shifts westward.

The asymmetry in the precipitation and zonal wind stress from the corresponding AMIP runs are first analyzed to understand the causes for the weaker ENSO asymmetry (or the weaker El Niño events) in CMIP5 coupled models. We found that mainly due to the weaker precipitation response to El Niño warming, most models have a weaker precipitation asymmetry over the eastern Pacific even driven by the observed SST forcing. This bias is further amplified in the coupled models that have a much weaker precipitation asymmetry over the eastern Pacific. During the warm phase, the weaker precipitation response over the eastern Pacific is accompanied by a stronger precipitation response over the central Pacific and linked to a westward shift of convection in the AMIP runs along with a clear westward shift of westerly wind anomaly. A westward shift of zonal wind stress during the warm phase in the AMIP runs may play a role in the weaker subsurface temperature warm anomalies in the coupled models (Kang and Kug 2002). Using two different coupled models to examine the sensitivity of ENSO amplitude to the convection scheme parameters, Watanabe et al. (2011) and Kim et al. (2011) showed that the parameter change in the cumulus parameterization shifts the position of the precipitation anomalies and the zonal wind stress also shifts accordingly. The increased eastern Pacific precipitation tends to shift the wind stress anomalies to the east. Closer to the eastern Pacific, the wind stress forcing more effectively deepens the thermocline over the eastern Pacific. Watanabe et al. (2011) have also showed that the subsurface temperature anomalies over the eastern Pacific are much stronger when the zonal wind stress shifts to the east. This is consistent with what we see from the CCSM4 model. The NCAR model, identified as the best model in simulating ENSO asymmetry,

509 has a realistic simulation of subsurface temperature warm anomalies associated with
510 sufficient precipitation response over the eastern Pacific in the AMIP run. An enhanced
511 precipitation response over the eastern Pacific during the warm phase is essential to the
512 improvement in the simulation of ENSO asymmetry in CMIP5 models, consistent with
513 the previous findings of Zhang et al. (2009).

514 We also find that most AMIP models have a stronger time-mean zonal wind over the
515 equatorial central and eastern Pacific, and underestimate the observed positive skewness
516 of zonal winds in the central Pacific. The bias in the mean zonal winds is more prominent
517 in the coastal regions over the eastern Pacific and the southern equatorial Pacific, where
518 the bias in mean precipitation is also evident in the AMIP runs. The mean precipitation
519 bias shows an east-west asymmetry. The latent heating asymmetry associated with the
520 stronger zonal precipitation gradient may generate the stronger zonal pressure gradient
521 force which then enhances the trade winds in the model (Lin 2007).

522 To understand the effect of the bias in the mean and interannual variability of winds
523 on ENSO asymmetry, forced ocean model experiments with the use of AMIP winds are
524 performed. These results are compared to those from the experiments forced by observed
525 winds. The numerical experiments show that when there is a colder mean SST state due
526 to the stronger mean winds in models, the biases in interannual anomalies of winds from
527 AMIP runs can weaken ENSO asymmetry by shifting SST warm anomalies westward
528 and reducing the magnitude. This is consistent with what we have seen in CMIP5
529 coupled models. The results from the run with full model winds confirm that the bias in
530 the SST anomalies during the warm phase is found to be the major cause for the
531 reduction in ENSO asymmetry. We note that with a warmer mean SST state, or when the

mean winds in models are the same as observations, the contribution to ENSO asymmetry from wind interannual variability bias is negligible. Also ENSO asymmetry is increased mainly due to the increase of SST warm anomalies. The results are consistent with those from an analytical model that the amplitude of warm events increases with enhanced radiative heating (Liang et al. 2012). This may also be useful to explain why coupled models tend to have a weaker ENSO asymmetry, given that the excessive cold tongue is still the problem in coupled models (Sun et al. 2006). These findings highlight the importance of a warmer mean SST state for ENSO asymmetry. Further studies are needed to explore this possible link.

To the extent a colder mean state of the ocean causes a weaker ENSO asymmetry and to the extent this colder mean state is mainly a consequence of the stronger zonal wind from the AMIP runs, our analysis pinpoints the causes of the weaker ENSO asymmetry in the coupled models to the stronger time-mean winds over the tropical Pacific in the stand-alone atmosphere model. Note that we have fully consider the momentum forcing (both zonal and meridional components) from AMIP model winds in the experimental design as an attempt to reveal the role of the bias in model winds more realistically. We have also performed additional ocean model experiments in which only zonal wind stress biases are considered. The results are found to be similar, suggesting a minor role of the biases in meridional wind stress as also noted in previous studies (McCreary 1976; Zhang and McPhaden 2006; Zhu et al. 2007).

## Acknowledgments

The authors acknowledge the support of the NOAA Climate Program Office Modeling, Analysis, Predictions and Projections (MAPP) Program as part of the CMIP5 Task Force. Work was supported under grant GC11-300.

559 **References:**


560 An, S.-I., and F.-F. Jin, 2004: Nonlinearity and asymmetry of ENSO. *J. Climate*, **17**,
561 2399–2412.

562 An, S-I., Y-G. Ham, J-S. Kug, F-F. Jin, and I-S. Kang, 2005: El Niño–La Niña
563 asymmetry in the Coupled Model Intercomparison Project simulations. *J. Climate*, **18,**
564 2617–2627.

565 An, S-I., 2009: A review of interdecadal changes in the nonlinearity of the El Nino-
566 Southern Oscillation. *Theor. Appl. Climatol.*, **97,** 29–40.

567 Burgers, G., and D. B. Stephenson, 1999: The "normality" of El Niño. *Geophys. Res.*
568 *Lett.*, **26,** 1027–1030.

569 Carton, J. A., and B. S. Giese, 2008: A reanalysis of ocean climate using Simple Ocean
570 Data Assimilation (SODA). *Mon. Wea. Rev.*, **136,** 2999–3017.

571 Carton, J. A., G. Chepurin, X. Cao, and B. Giese, 2000: A simple ocean data assimilation
572 analysis of the global upper ocean 1950–95. Part I: Methodology. *J. Phys. Oceanogr.*,
573 **30,** 294–309.

574 Chung, P.-H., and T. Li, 2013: Interdecadal Relationship between the Mean State and El
575 Niño Types. *J. Climate*, **26**, 361–379.

576 Deser, Clara, A. S. Phillips, R. A. Tomas, Y. M. Okumura, M. A. Alexander, A.
577 Capotondi, J. D. Scott, Y.-O. Kwon, and M. Ohba, 2012: ENSO and Pacific Decadal
578 Variability in the Community Climate System Model Version 4. *J. Climate*, **25**,
579 2622–2651.

580 Gent, Peter R., G. Danabasoglu, L. J. Donner, M. M. Holland, E. C. Hunke, S. R. Jayne,
581 D. M. Lawrence, R. B. Neale, P. J. Rasch, M. Vertenstein, P. H. Worley, Z.-L. Yang,

582 and M. Zhang, 2011: The Community Climate System Model Version 4. *J. Climate*,
583 **24**, 4973–4991.
584 Gent, P. R., and M. A. Cane, 1989: A reduced gravity, primitive equation model of the
585 upper equatorial ocean, *J. Comput. Phys*., **81**, 444–480.
586 Hannachi, A., D. Stephenson, and K. Sperber, 2003: Probability-based methods for
587 quantifying nonlinearity in the ENSO. *Climate Dyn.*, **20,** 241–256.
588 Hoerling M. P., A. Kumar, and M. Zhong, 1997: El Niño, La Niña, and the nonlinearity
589 of their teleconnections. *J. Climate*, **10**, 1769–1786.
590 Jin, F.-F., S.-I. An, A. Timmermann, and J. Zhao, 2003: Strong El Niño events and
591 nonlinear dynamical heating, *Geophys. Res. Lett*., **30**(3), 1120,
592 doi:10.1029/2002GL016356.
593 Kang, I-S., and J-S. Kug, 2002: El Niño and La Niña sea surface temperature anomalies:
594 Asymmetry characteristics associated with their wind stress anomalies. *J. Geophys.*
595 *Res.*, **107,** 4372. doi:10.1029/2001JD000393.
596 Kiladis, G. N., and H. Diaz, 1989: Global climatic anomalies associated with extremes in
597 the Southern Oscillation. *J. Climate,* **2,** 1069–1090.
598 Kim, D., Y.-S. Jang, D.-H. Kim, Y.-H. Kim, M. Watanabe, F.-F. Jin, and J.-S. Kug
599 (2011), El Niño–Southern Oscillation sensitivity to cumulus entrainment in a coupled
600 general circulation model, *J. Geophys. Res.*, **116**, D22112,
601 doi:10.1029/2011JD016526.
602 Larkin, N. K., and D. E. Harrison, 2005: On the definition of El Niño and associated
603 seasonal average U.S. weather anomalies. *Geophys. Res. Lett.,* **32**, L13705,
604 doi:10.1029/2005GL022738.

605 Liang, J., X.-Q. Yang, and D.-Z. Sun, 2012: The effect of ENSO events on the Tropical
606 Pacific Mean Climate: Insights from an Analytical Model. *J. Climate*, **25**, 7590–7606.
607 Lin, J.-L., 2007: The Double-ITCZ Problem in IPCC AR4 Coupled GCMs: Ocean–
608 Atmosphere Feedback Analysis. *J. Climate*, **20**, 4497–4525.
609 McCreary, J., 1976: Eastern tropical ocean response to changing wind systems: With
610 application to El Niño. *J. Phys. Oceanogr.*, **6,** 632–645.
611 McPhaden, M. J., T. Lee, and D. McClurg, 2011: El Niño and its relationship to changing
612 background conditions in the tropical Pacific Ocean. *Geophys. Res. Lett.*, **38**, L15709,
613 doi:10.1029/2011GL048275.
614 Neale, R. B., J. H. Richter, and M. Jochum, 2008: The impact of convection on ENSO:
615 From a delayed oscillator to a series of events. *J. Climate*, **21,** 5904–5924.
616 Rayner, N. A., D. E. Parker, E. B. Horton, C. K. Folland, L. V. Alexander, D. P. Rowell,
617 E. C. Kent, and A. Kaplan, 2003: Global analyses of sea surface temperature, sea ice
618 and night marine air temperature since the late nineteenth century. *J. Geophys. Res.*,
619 **108,** 4407. doi:10.1029/2002JD002670.
620 Rodgers, K. B., P. Friederichs, and M. Latif, 2004: Tropical Pacific decadal variability
621 and its relation to decadal modulation of ENSO. *J. Climate*, **17,** 3761–3774.
622 Ropelewski, C. F., and M. S. Halpert, 1987: Global and regional scale precipitation
623 patterns associated with the El Niño/ Southern Oscillation. *Mon. Wea. Rev.,* **115,**
624 1606–1626.
625 Schopf, P. S., and R. J. Burgman, 2006: A simple mechanism for ENSO residuals and
626 asymmetry. *J. Climate*, **19,** 3167–3179.
627 Su, J., R. Zhang, T. Li, X. Rong, J.-S. Kug, and C.-C. Hong, 2010: Causes of the El Niño

628 and La Niña amplitude asymmetry in the equatorial eastern Pacific, *J. Climate*, **23**,
629 605–617, doi:10.1175/2009JCLI2894.1.
630 Sun, D.-Z., and T. Zhang, 2006: A regulatory effect of ENSO on the time-mean thermal
631 stratification of the equatorial upper ocean. *Geophys. Res. Lett.*, **33,** L07710.
632 doi:10.1029/2005GL025296.
633 Sun, D.-Z., T. Zhang, C. Covey, S. Klein, W. Collins, J. Hack, J. Kiehl, G.A. Meehl, I.
634 Held, and M. Suarez, 2006: Radiative and Dynamical Feedbacks Over the Equatorial
635 Cold Tongue: Results from Nine Atmospheric GCMs. *J. Climate*, **19**, 4059-4074.
636 Sun, D.-Z., 2003: A possible effect of an increase in the warm-pool SST on the
637 magnitude of El Niño warming, *J. Climate*, **16**, 185–205.
638 Sun, D.-Z. and F. Bryan (eds), 2010: Climate Dynamics: Why Does Climate Vary?. AGU
639 Monograph, 216 pages, AGU.
640 Sun, D.-Z., T. Zhang, Y. Sun, and Y. Yu, 2014: Rectification of El Niño-Southern
641 Oscillation into Climate Anomalies of Decadal and Longer Time-scales: Results from
642 Forced Ocean GCM Experiments. *J. Climate*, in press.
643 Sun, D.-Z., T. Zhang, and S.-I. Shin, 2004: The effect of subtropical cooling on the
644 amplitude of ENSO: A numerical study, *J. Climate*, **17**, 3786– 3798.
645 Sun, F., and J-Y. Yu, 2009: A 10–15-year modulation cycle of ENSO intensity. *J.*
646 *Climate*, **22,** 1718–1735.
647 Sun, Y., D.-Z. Sun, L. X. Wu, and F. Wang, 2013: Western Pacific Warm Pool and
648 ENSO Asymmetry in CMIP3 Models. *Adv. Atmos. Sci.*, **30**(3), 940–953, doi:
649 10.1007/s00376-012-2161-1.
650 Taylor, K. E., R. J. Stouffer, and G. A. Meehl, 2012: An overview of CMIP5 and the

experiment design, *Bull. Am. Meteorol. Soc.,* **93**, 485–498, doi:10.1175/BAMS-D-11-00094.1.

van Oldenborgh, G. J., S. Philip, and M. Collins, 2005: El Niño in a changing climate: A multi-model study. *Ocean Sci.,* **1,** 81–95.

Vialard, J., C. Menkes, J-P. Boulanger, P. Delecluse, E. Guilyardi, M. J. McPhaden, and G. Madec, 2001: A model study of oceanic mechanisms affecting equatorial Pacific sea surface temperature during the 1997–98 El Niño. *J. Phys. Oceanogr.*, **31,** 1649–1675.

Watanabe, M., M. Chikira, Y. Imada, and M. Kimoto (2011), Convective control of ENSO simulated in MIROC, *J. Climate*, **24**, 543–562, doi:10.1175/2010JCLI3878.1.

Xie, P., and P. A. Arkin, 1997: Global precipitation: A 17-year monthly analysis based on gauge observations, satellite estimates, and numerical model outputs. *Bull. Amer. Meteor. Soc.*, **78,** 2539–2558.

Zhang, G. J., and N. A. McFarlane, 1995: Sensitivity of climate simulations to the parameterization of cumulus convection in the Canadian Climate Centre general circulation model. *Atmos.–Ocean*, **33,** 407–446.

Zhang, T., D.-Z. Sun, R. Neale, and P. J. Rasch, 2009: An Evaluation of ENSO Asymmetry in the Community Climate System Models: A View from the Subsurface. *J. Climate*, **22**, 5933-5961.

Zhang, T., M. P. Hoerling, J. Perlwitz, D.-Z. Sun, and D. Murray, 2011: Physics of U.S. surface temperature response to ENSO. *J. Climate*, **24**, 4874–4887.

672 Zhang, T., J. Perlwitz, and M. P. Hoerling, 2013: What is Responsible for the Strong
673 Observed Asymmetry in Teleconnections Between El Niño and La Niña? *Geophys.*
674 *Res. Lett.*, Submitted.
675 Zhang, X., and M. J. McPhaden, 2006: Wind stress variations and interannual sea surface
676 temperature anomalies in the eastern equatorial Pacific. *J. Climate*, **19**, 226–241.
677 Zhu, J., Z. Sun, and G. Zhou, 2007: A note on the role of meridional wind stress
678 anomalies and heat flux in ENSO simulations. *Adv. Atmos. Sci.*, **24**(4), 729–738, doi:
679 10.1007/s00376-007-0729-y.
680

## Table and Figure Captions

Table 1: Standard deviation and skewness of the interannual variability in Niño-3 SST from four forced ocean model experiments. The mean as well as the anomaly part of the surface winds used in these experiments are listed. The length of observed wind data used in the forced runs is 30-year for SODA wind stress (1979–2008). The length of simulated wind data used is 27-year for CAM4 (1979-2005) and 30-year for other models (1979-2008).

Figure 1: Standard deviation (upper) and skewness (bottom) of the interannual variability in Niño-3 SST from observations and CMIP5 coupled models. The length of data used in the calculation is 50 years for all the models and observations (1950-99).

Figure 2: The sum of the composite SST anomalies between the two phases of ENSO from observations and CMIP5 coupled models. Following the study of Zhang et al. (2009), the positive (negative) anomalies of Niño-3 SST with a value greater than 0.5°C (−0.5°C) are selected to construct composites of warm (cold) events. Same data used as for Figure 1.

Figure 3: The sum of the composite equatorial ($5^oS$-$5^oN$) upper ocean temperature anomalies between the two phases of ENSO from observations and CMIP5 coupled models. The length of data used in the calculation is 50 years for all the models and SODA data (1950-1999).

Figure 4: Composite SST anomalies for the warm phase of ENSO from observations and coupled models.

Figure 5: Composite anomalies of equatorial ($5^{o}$S-$5^{o}$N) upper ocean temperature for the warm phase of ENSO from observations and coupled models.

Figure 6: The difference between observations and ensemble mean composite SST anomalies for warm phase of ENSO (top), the difference between observations and ensemble mean composite SST anomalies for cold phase of ENSO (middle), and the difference between observations and ensemble mean SST annual climatology (bottom) from fourteen CMIP5 coupled models.

Figure 7: The sum of the composite anomalies for the two phases of ENSO for precipitation (shaded) and zonal wind stress (contours) from observations and CMIP5 coupled models. The length of data used in the calculation is 50 years for all the models, 30 years for CMAP precipitation (1979–2008), and 50 years for SODA zonal wind stress (1959–2008).

Figure 8: The sum of the composite precipitation anomalies between the two phases of ENSO from observations and the corresponding AMIP runs of CMIP5 coupled models. The length of data used in the calculation is 30 years for CMAP precipitation (1979–2008), 27 years for CAM4 (1979-2005) and 30 years for the other models (1979-2008).

727 Figure 9: The sum of the composite precipitation anomalies of the two phases of ENSO
728 averaged over the eastern Pacific (120°W-70°W, 10°S-10°N) from CMIP5 coupled
729 models (top panel) and the corresponding AMIP runs (bottom panel). The corresponding
730 observational value is also included in the figures. The length of data used in the
731 calculation is 30 years for CMAP precipitation (1979–2008), and 50 years for all the
732 coupled models. The length of data used for AMIP runs is the same as for Figure 8.
733
734 Figure 10: Composite precipitation anomalies for the warm phase of ENSO averaged
735 over the eastern Pacific (120°W-70°W, 10°S-10°N) from CMIP5 coupled models (top
736 panel) and the corresponding AMIP runs (bottom panel).
737
738 Figure 11: The warm phase precipitation anomalies (left panel) and zonal wind stress
739 anomalies (right panel) from observations, the ensemble mean of the model results, and
740 their differences. Green lines indicate the positions that the equatorial westerly wind
741 anomaly can reach. Fourteen CMIP5 AMIP runs during the warm phase are used in
742 calculating the ensemble mean. The length of observational data used in the calculation is
743 30 years for CMAP precipitation and SODA zonal wind stress (1979–2008). The length
744 of data used for AMIP runs is the same as for Figure 8.
745
746 Figure 12: The time-mean zonal wind stress (top) over the equatorial central and eastern
747 Pacific (170°E-70°W, 5°S-5°N) and the skewness of the interannual anomalies of the
748 zonal wind stress (bottom) over the central Pacific (160°E-140°W, 10°S-5°N) from
749 observations and CMIP5 AMIP runs. The ensemble mean of the results from fourteen

AMIP runs is also included in the figure. Monthly anomalies are used to calculate the skewness. The length of observational data used in the calculation is 30 years for SODA zonal wind stress (1979–2008). The length of data used for AMIP runs is the same as for Figure 8.

Figure 13: The difference between observations and the ensemble mean zonal wind stress annual climatology (top) and the difference between observations and ensemble mean precipitation annual climatology (bottom) from fourteen CMIP5 AMIP runs. The length of observational data used in the calculation is 30 years for CMAP precipitation and SODA zonal wind stress (1979–2008). The length of data used for AMIP runs is the same as for Figure 8.

Figure 14: The sum of the composite anomalies of the two phases of ENSO for SST (left panel) and the equatorial ($5^{o}$S-$5^{o}$N) upper ocean temperature (right panel) in the four forced ocean experiments as listed in Table 1.

Figure 15: Composite anomalies of SST (left panel) and the equatorial ($5^{o}$S-$5^{o}$N) upper ocean temperature (right panel) for the warm phase of ENSO in the four forced ocean experiments as listed in Table 1.

Figure 16: Composite anomalies of SST (left panel) and the equatorial ($5^{o}$S-$5^{o}$N) upper ocean temperature (right panel) for the cold phase of ENSO in the four forced ocean experiments as listed in Table 1.

773

774 Figure 17: Time mean SST difference (left panel) and the equatorial ($5^{o}$S-$5^{o}$N) upper

775 ocean temperature difference (right panel) of Experiment II, Experiment III, and

776 Experiment IV from Experiment I.

777

Table 1: Standard deviation and skewness of the interannual variability in Niño-3 SST from four forced ocean model experiments. The mean as well as the anomaly part of the surface winds used in these experiments are listed. The length of observed wind data used in the forced runs is 30 years for SODA wind stress (1979–2008). The length of simulated wind data used is 27 years for CAM4 (1979-2005) and 30 years for other models (1979-2008).

| Experiment ID (label in figures) | Surface wind stress | | Statistics of Nino3 SSTA | |
|---|---|---|---|---|
| | Climatology | Anomaly | Skewness | Standard deviation( $^{O}$C) |
| Experiment I | Observation | Observation | 1.16 | 0.75 |
| | | | | |
| Experiment II | CMIP5 amip ensemble | Observation | 0.92 | 0.73 |
| | | | | |
| Experiment III | CMIP5 amip ensemble | CMIP5 amip ensemble | 0.70 | 0.63 |
| | | | | |
| Experiment IV | Observation | CMIP5 amip ensemble | 1.18 | 0.64 |

804

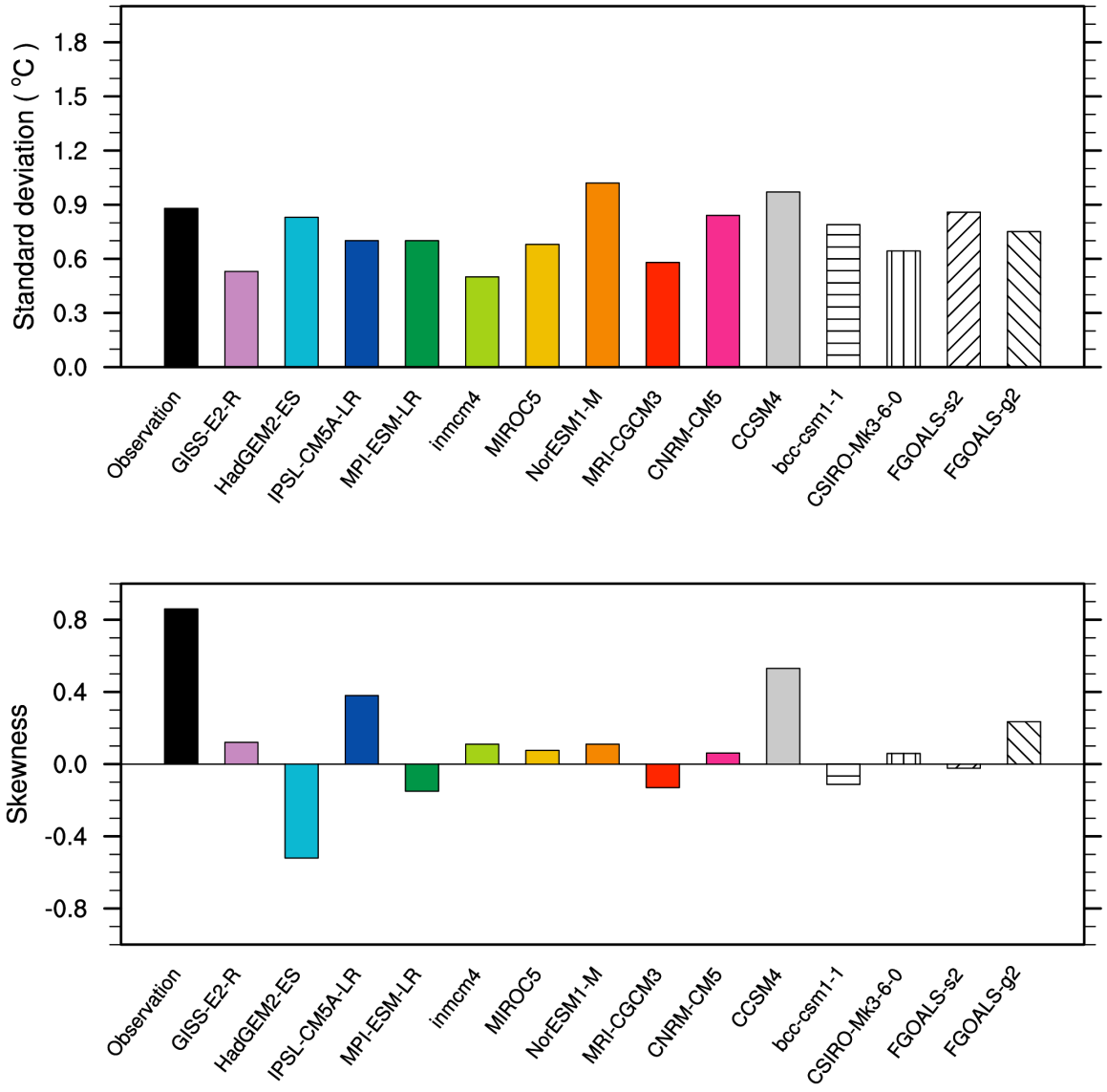


805
806
807
808
809
810
811
812
813
814
815
816
817
818
819

Figure 1: Standard deviation (upper) and skewness (bottom) of the interannual variability in Niño-3 SST from observations and CMIP5 coupled models. The length of data used in the calculation is 50 years for all the models and observations (1950-99).

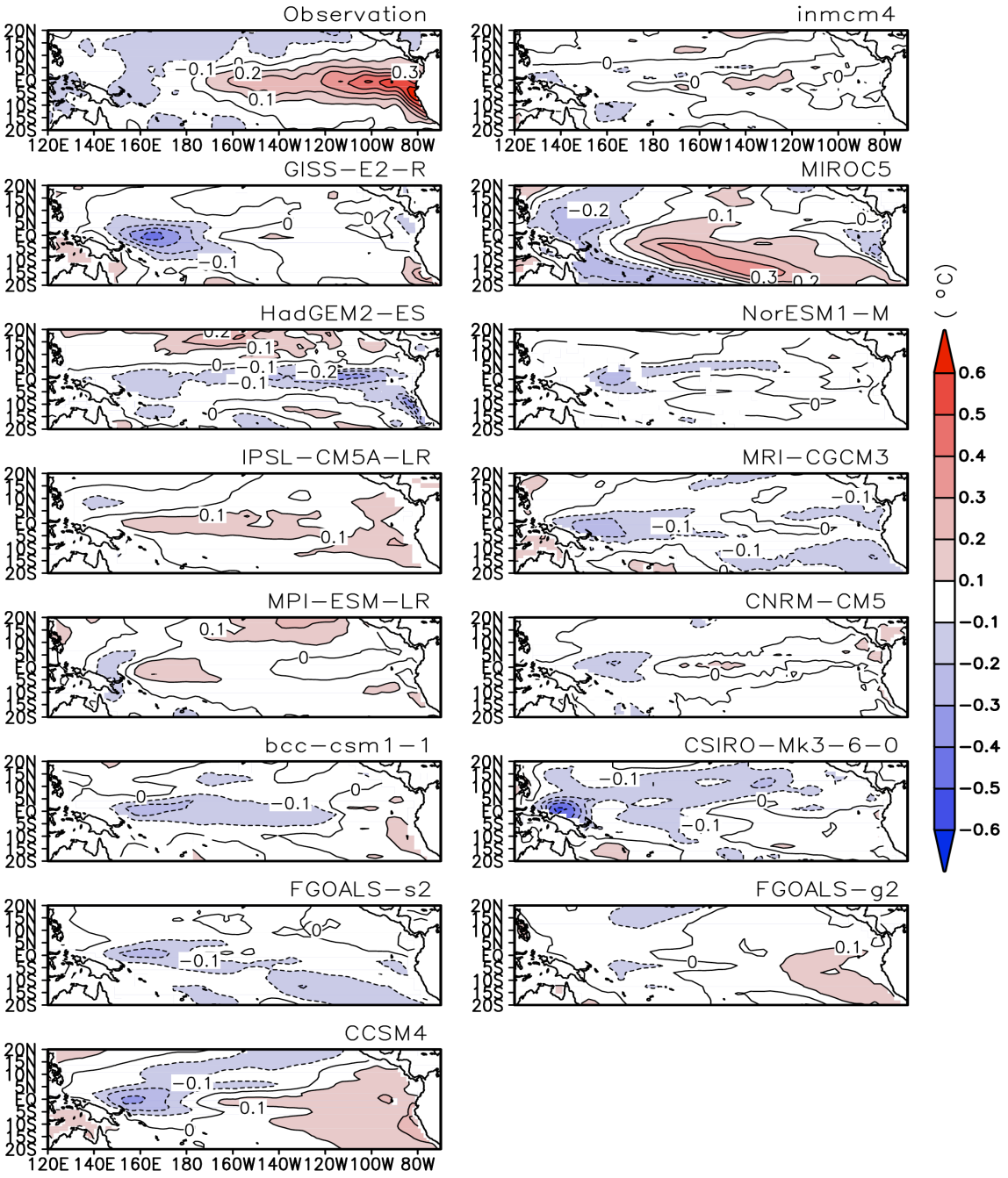


Figure 2: The sum of the composite SST anomalies between the two phases of ENSO from observations and CMIP5 coupled models. Following the study of Zhang et al. (2009), the positive (negative) anomalies of Niño-3 SST with a value greater than 0.5°C (−0.5°C) are selected to construct composites of warm (cold) events. Same data used as for Figure 1.

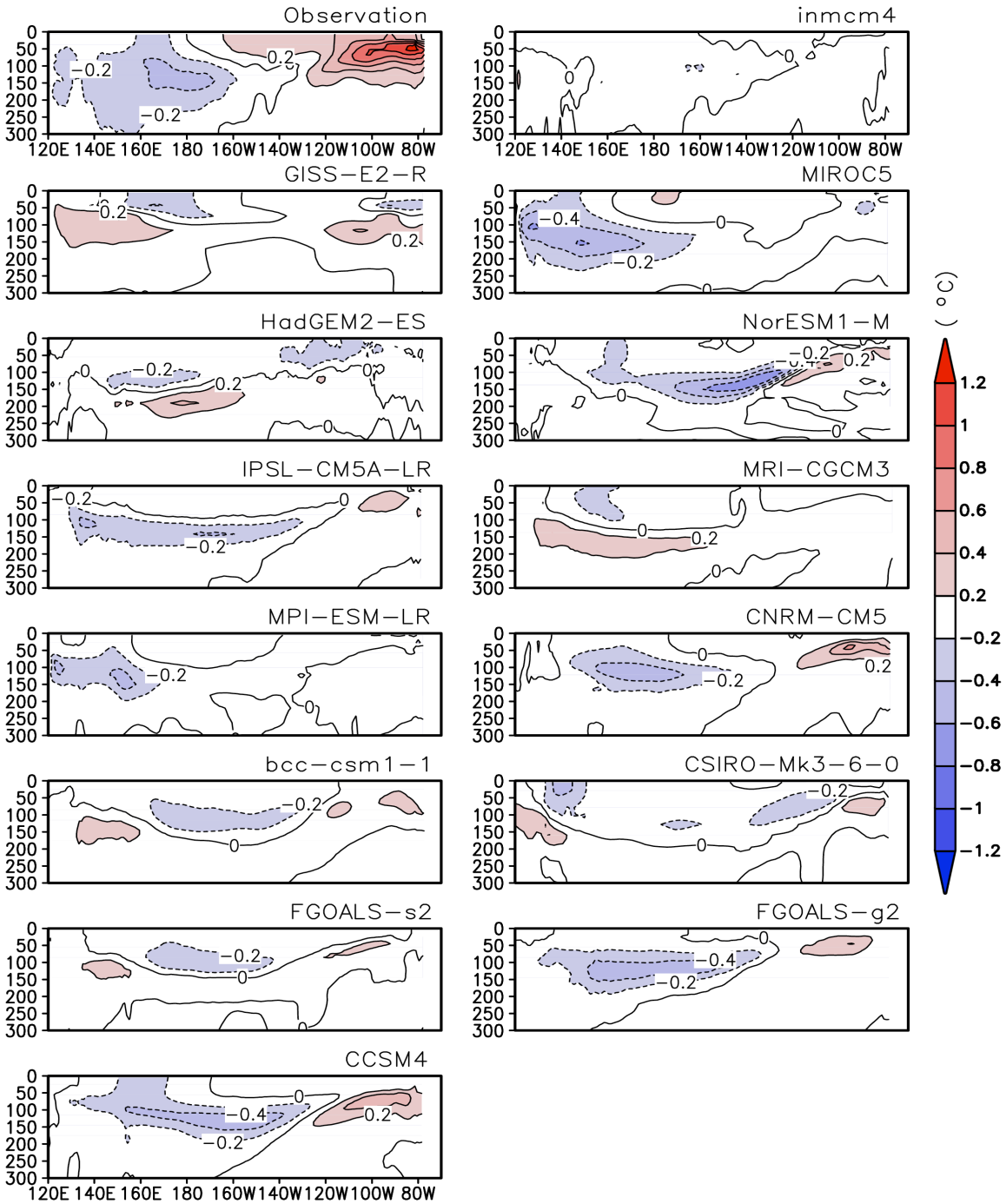


Figure 3: The sum of the composite equatorial (5°S-5°N) upper ocean temperature anomalies between the two phases of ENSO from observations and CMIP5 coupled models. The length of data used in the calculation is 50 years for all the models and SODA data (1950-1999).

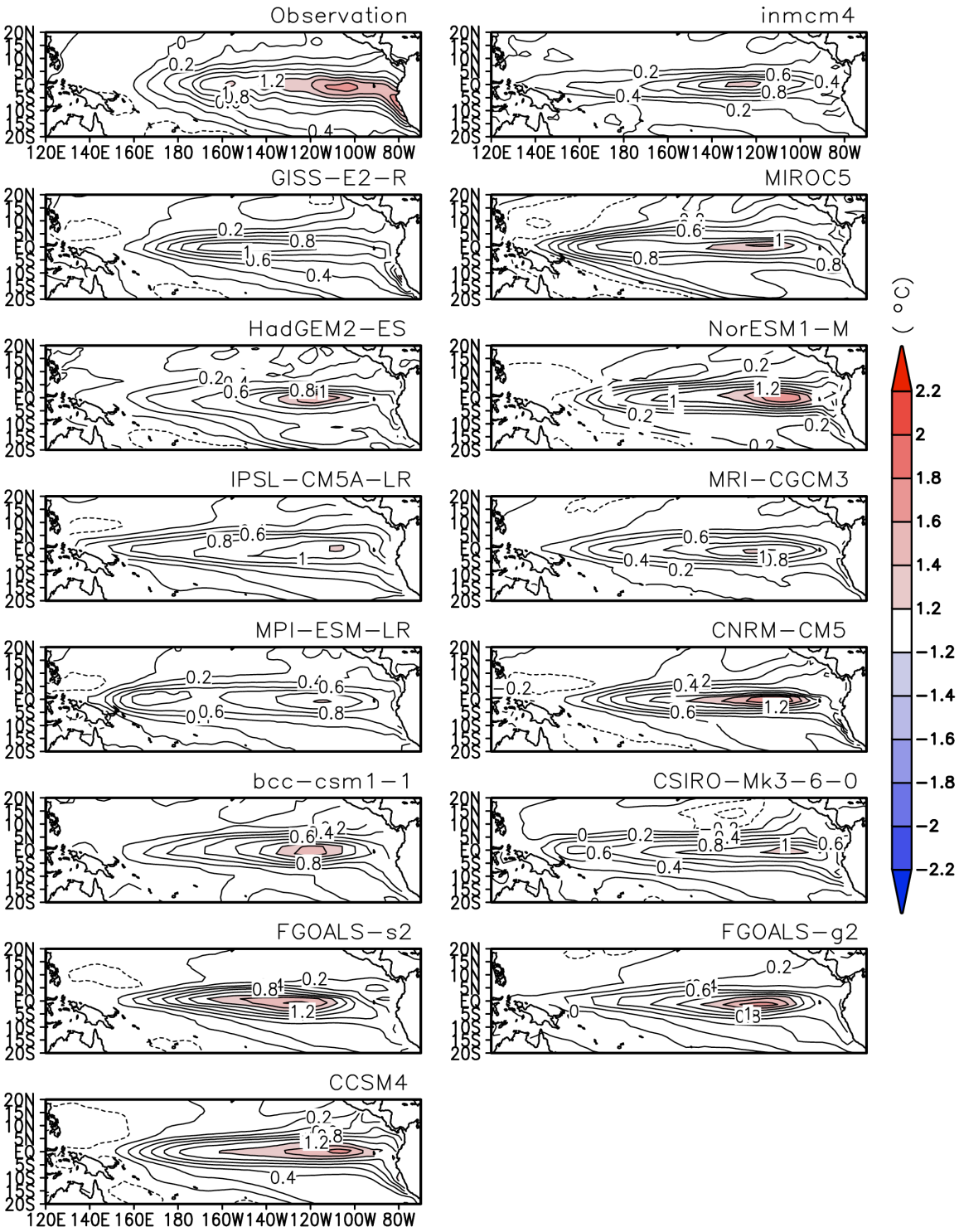


Figure 4: Composite SST anomalies for the warm phase of ENSO from observations and coupled models.

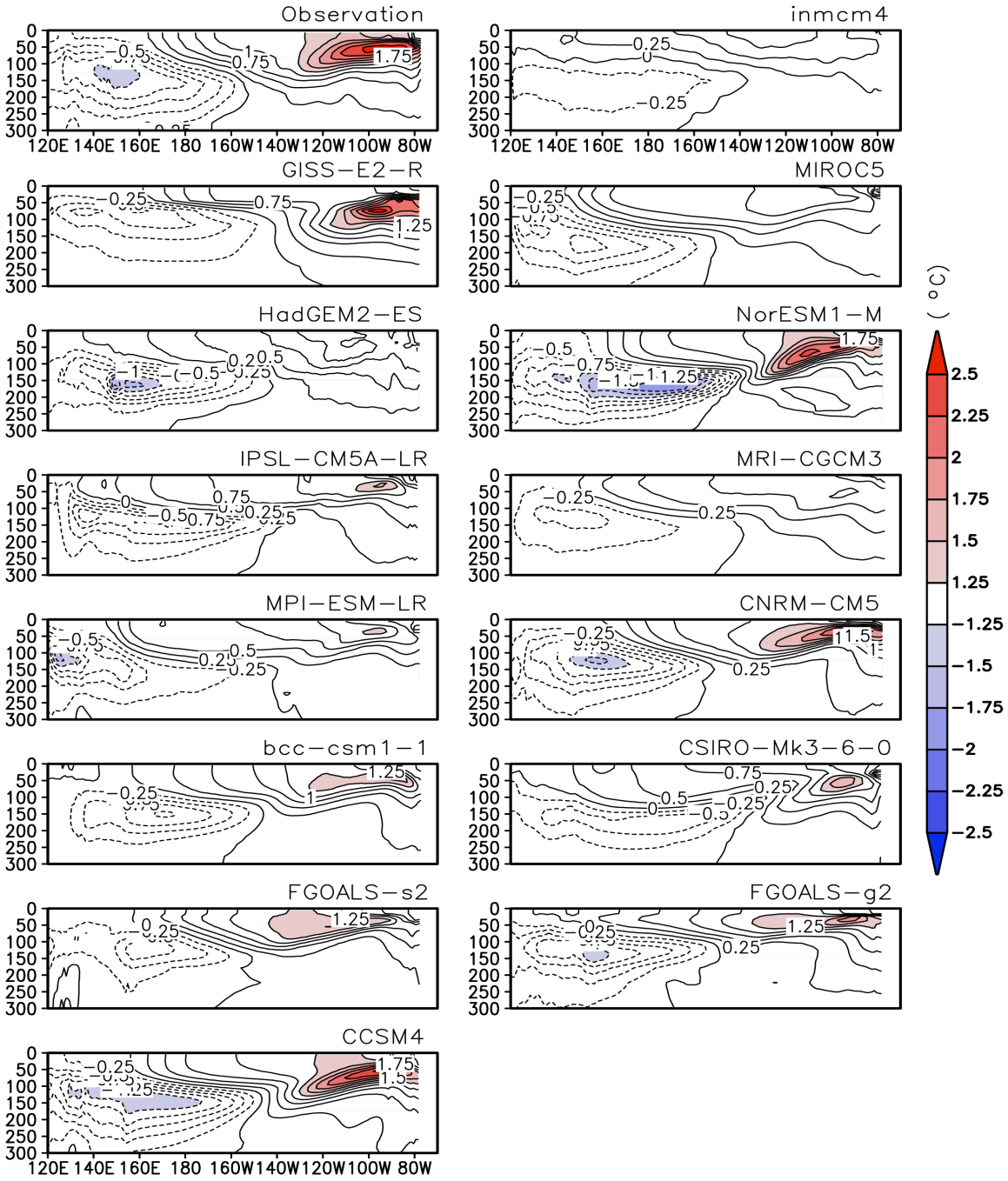


Figure 5: Composite anomalies of equatorial (5°S-5°N) upper ocean temperature for the warm phase of ENSO from observations and coupled models.

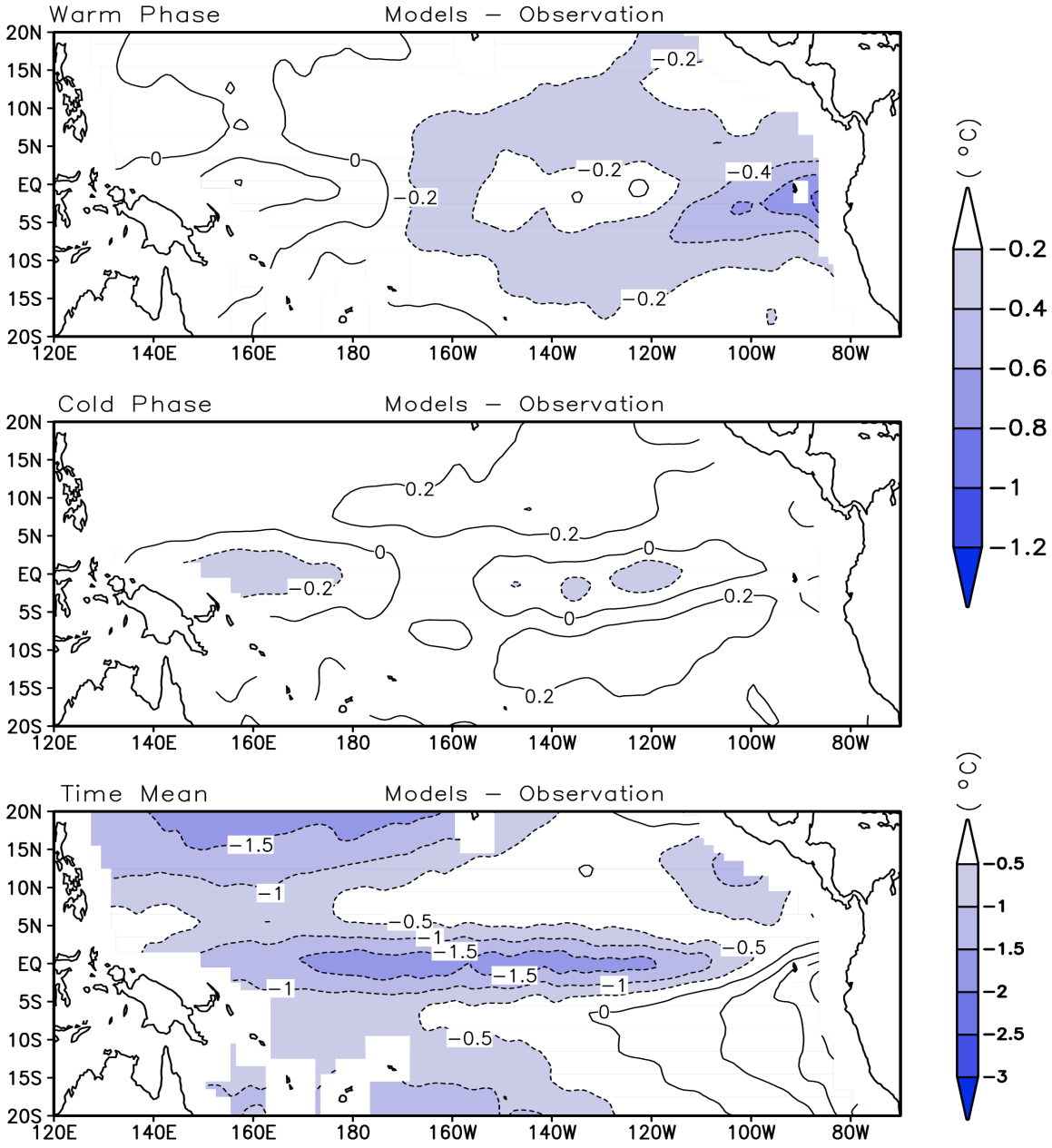


Figure 6: The difference between observations and ensemble mean composite SST anomalies for warm phase of ENSO (top), the difference between observations and ensemble mean composite SST anomalies for cold phase of ENSO (middle), and the difference between observations and ensemble mean SST annual climatology (bottom) from fourteen CMIP5 coupled models.

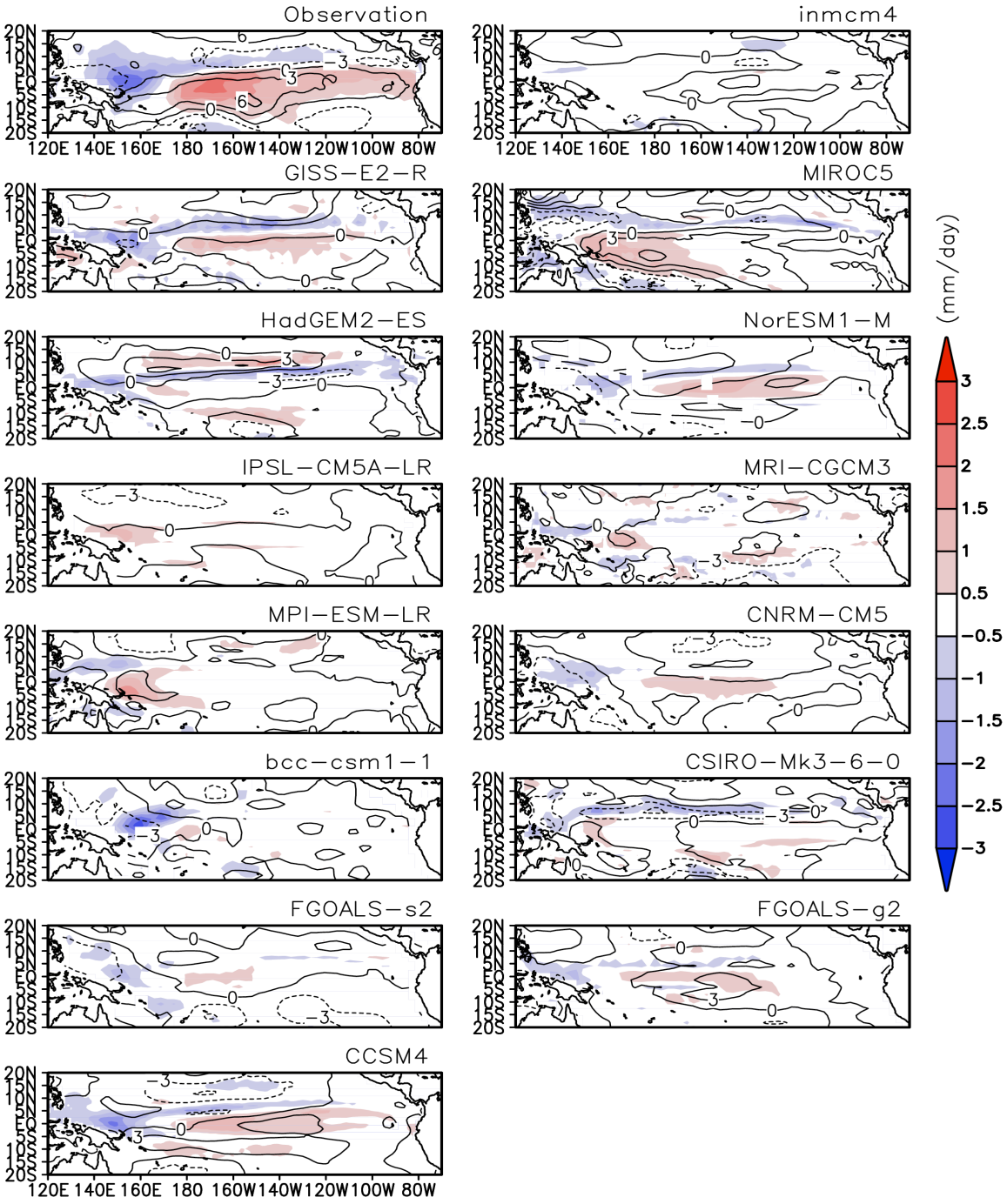


Figure 7: The sum of the composite anomalies for the two phases of ENSO for precipitation (shaded) and zonal wind stress (contours) from observations and CMIP5 coupled models. The length of data used in the calculation is 50 years for all the models, 30 years for CMAP precipitation (1979–2008), and 50 years for SODA zonal wind stress (1959–2008).

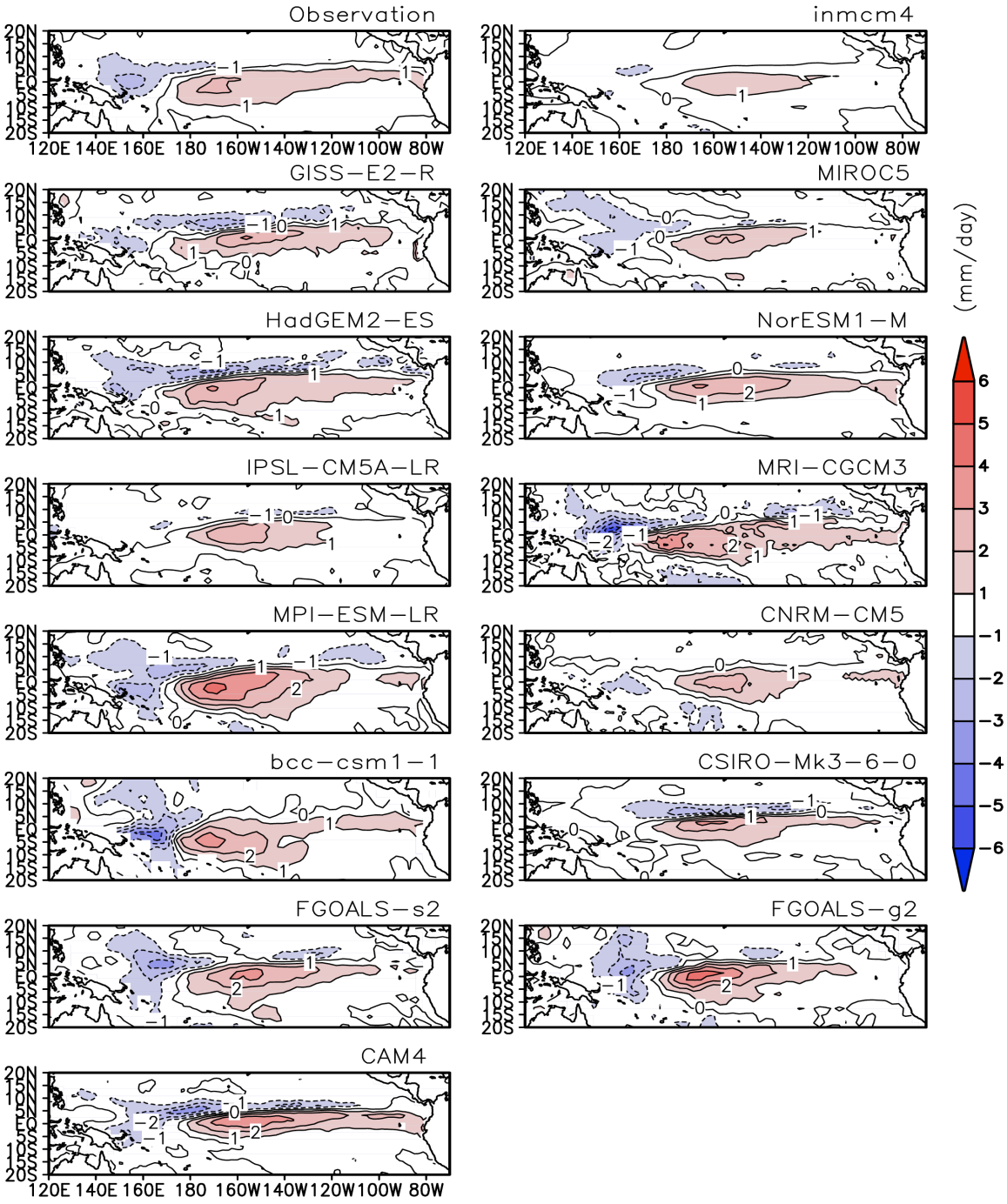


Figure 8: The sum of the composite precipitation anomalies between the two phases of ENSO from observations and the corresponding AMIP runs of CMIP5 coupled models. The length of data used in the calculation is 30 years for CMAP precipitation (1979–2008), 27 years for CAM4 (1979-2005) and 30 years for the other models (1979-2008).

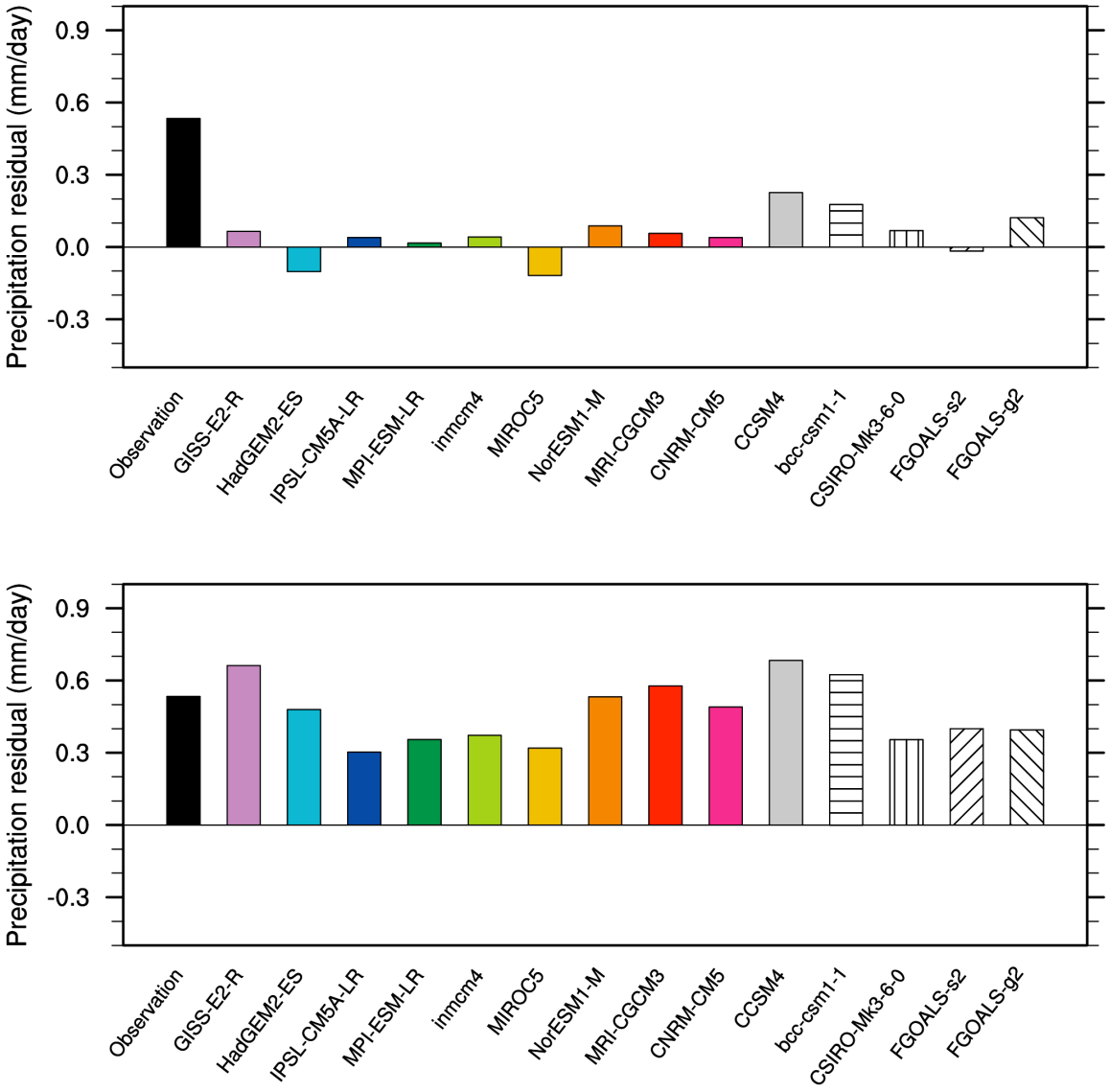


Figure 9: The sum of the composite precipitation anomalies of the two phases of ENSO averaged over the eastern Pacific (120°W-70°W, 10°S-10°N) from CMIP5 coupled models (top panel) and the corresponding AMIP runs (bottom panel). The corresponding observational value is also included in the figures. The length of data used in the calculation is 30 years for CMAP precipitation (1979–2008), and 50 years for all the coupled models. The length of data used for AMIP runs is the same as for Figure 8.

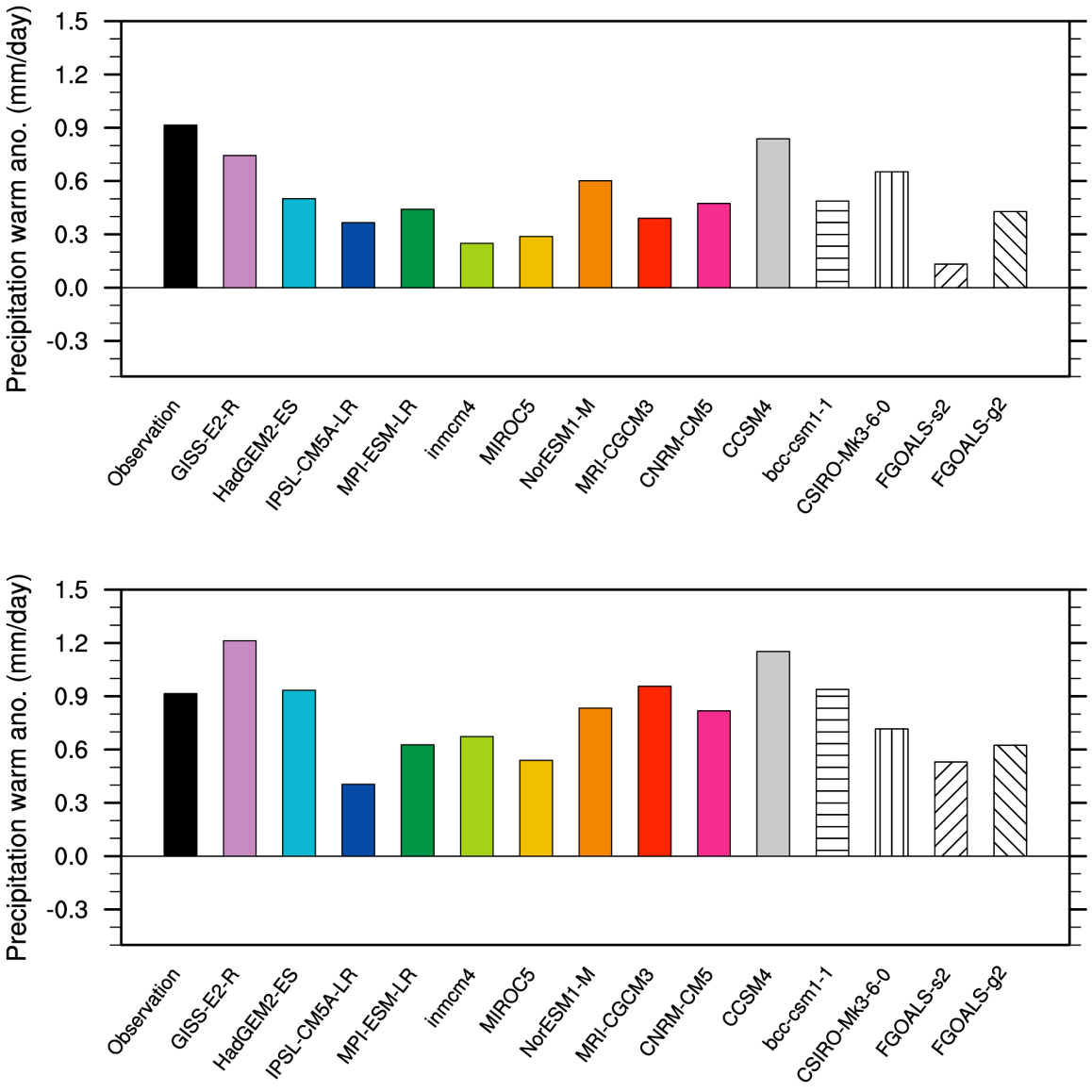


Figure 10: Composite precipitation anomalies for the warm phase of ENSO averaged over the eastern Pacific (120°W-70°W, 10°S-10°N) from CMIP5 coupled models (top panel) and the corresponding AMIP runs (bottom panel).

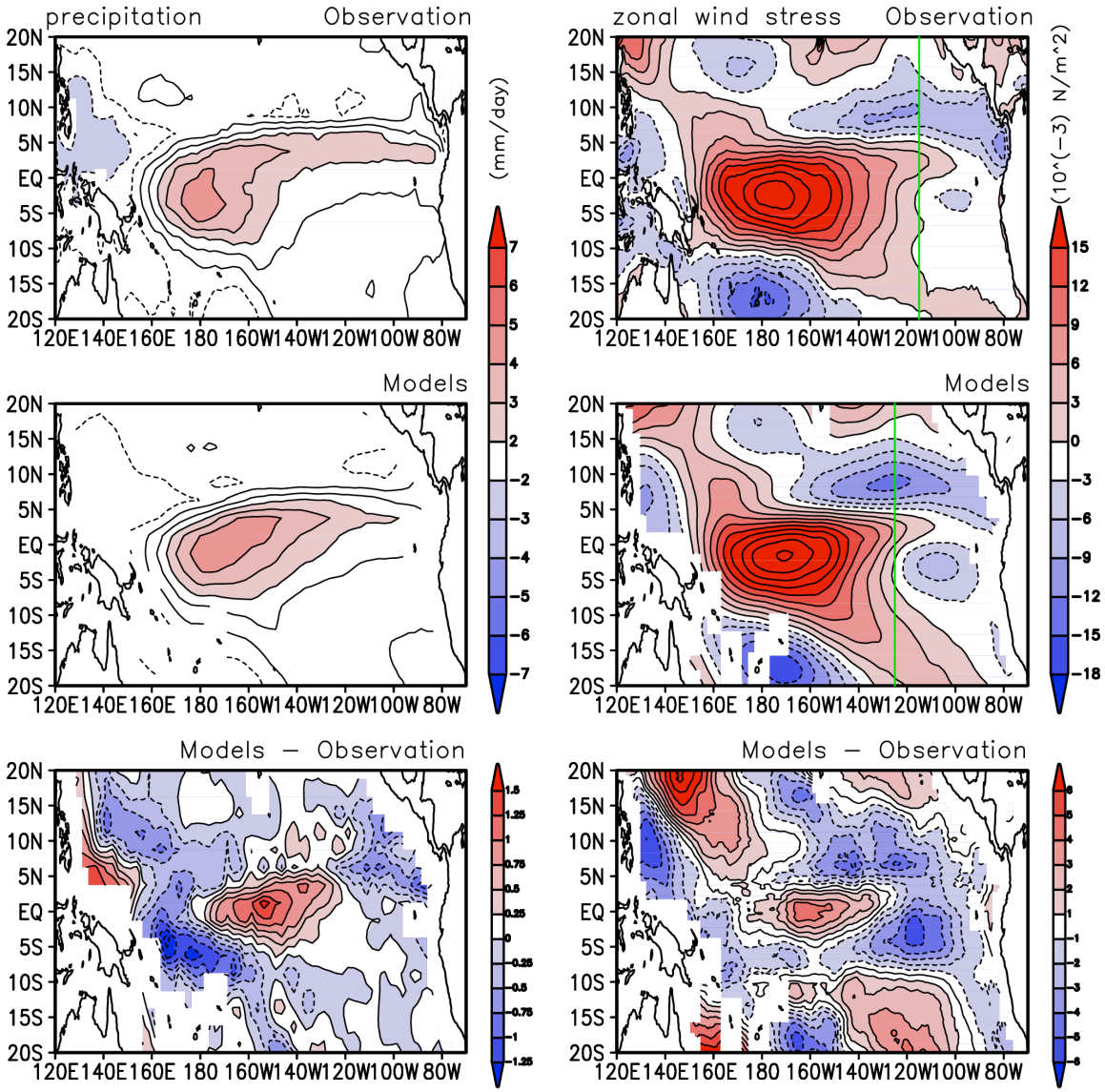


Figure 11: The warm phase precipitation anomalies (left panel) and zonal wind stress anomalies (right panel) from observations, the ensemble mean of the model results, and their differences. Green lines indicate the positions that the equatorial westerly wind anomaly can reach. Fourteen CMIP5 AMIP runs during the warm phase are used in calculating the ensemble mean. The length of observational data used in the calculation is 30 years for CMAP precipitation and SODA zonal wind stress (1979–2008). The length of data used for AMIP runs is the same as for Figure 8.

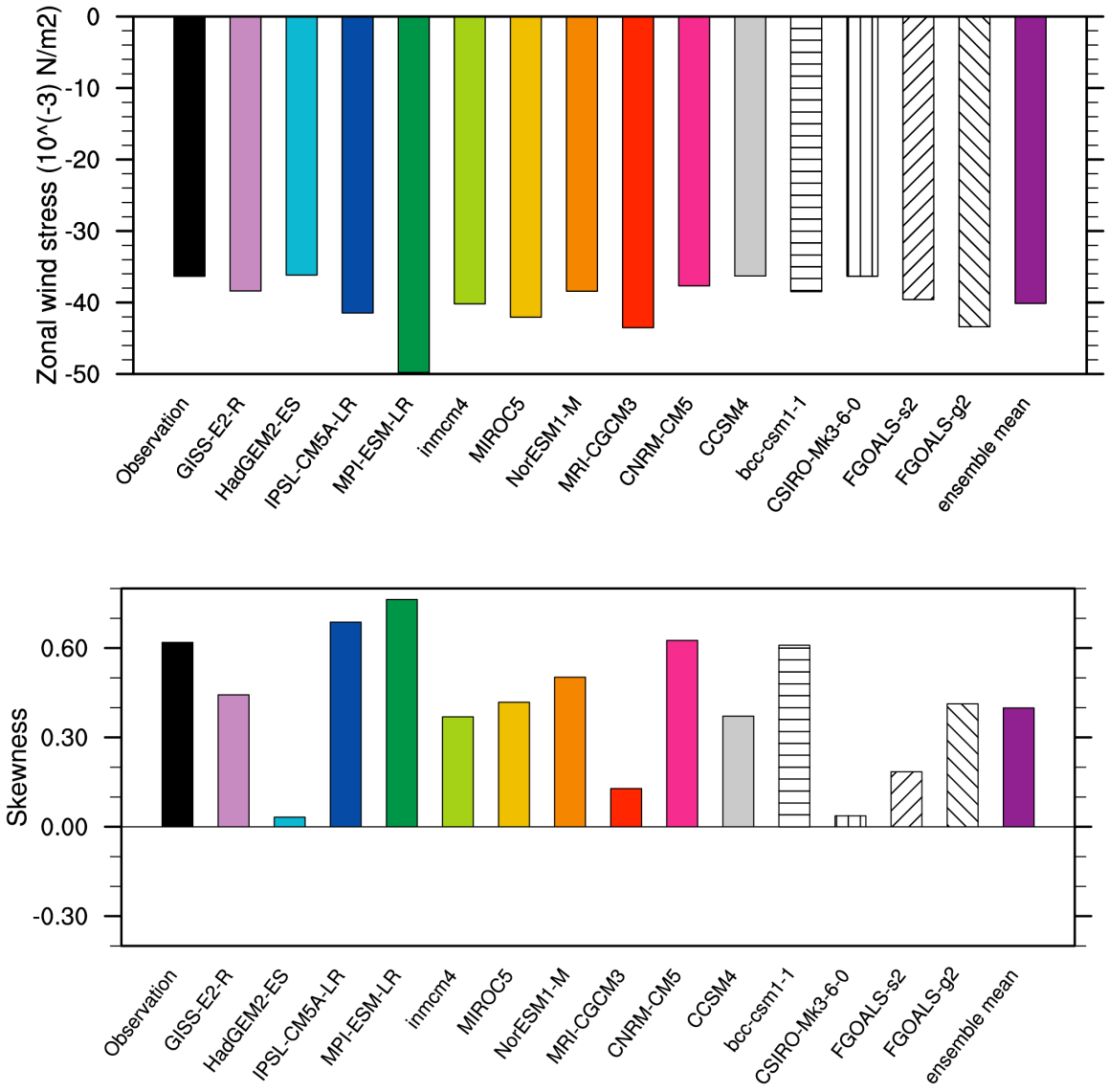


Figure 12: The time-mean zonal wind stress (top) over the equatorial central and eastern Pacific (170°E-70°W, 5°S-5°N) and the skewness of the interannual anomalies of the zonal wind stress (bottom) over the central Pacific (160°E-140°W, 10°S-5°N) from observations and CMIP5 AMIP runs. The ensemble mean of the results from fourteen AMIP runs is also included in the figure. Monthly anomalies are used to calculate the skewness. The length of observational data used in the calculation is 30 years for SODA zonal wind stress (1979–2008). The length of data used for AMIP runs is the same as for Figure 8.

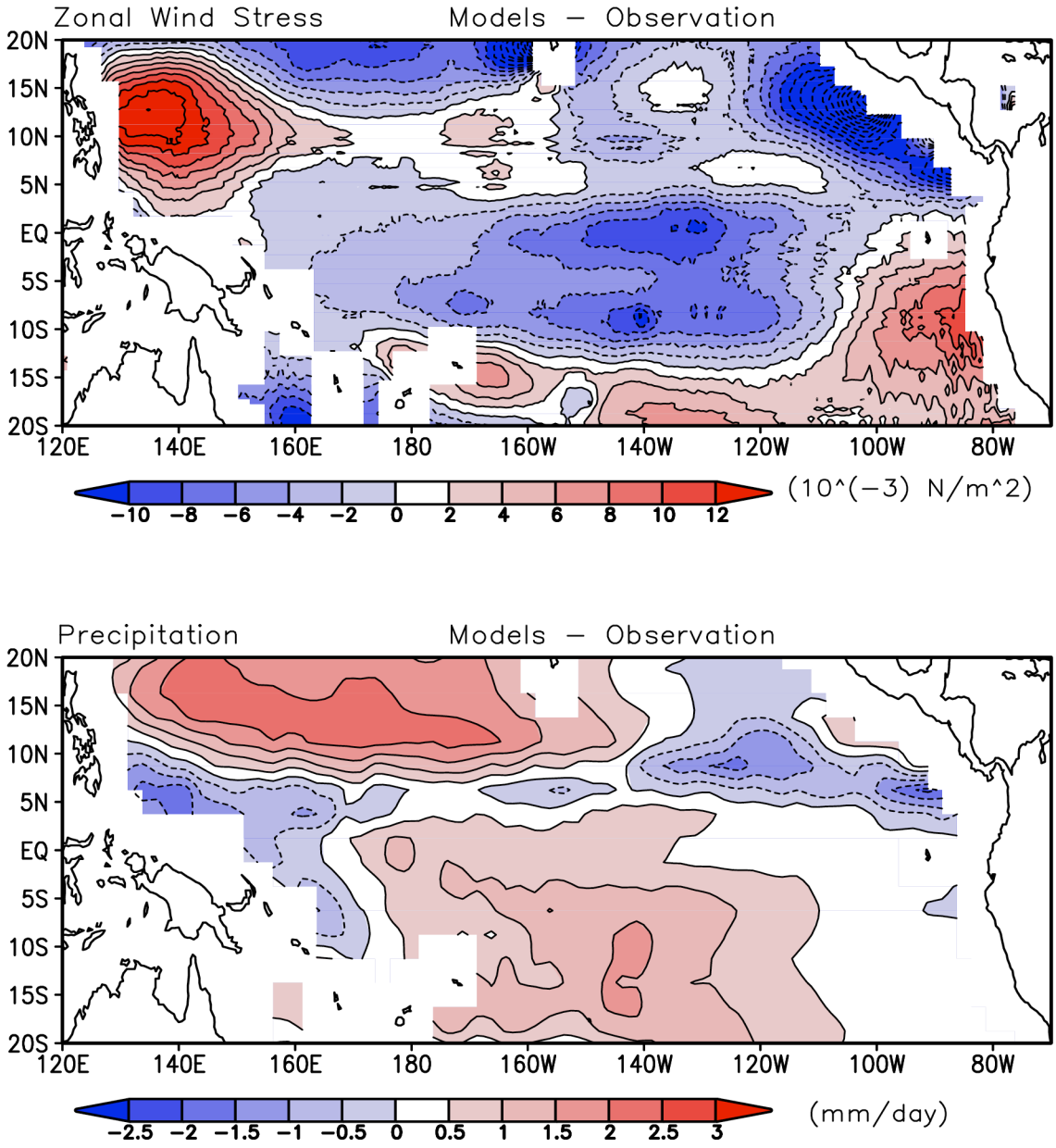


Figure 13: The difference between observations and the ensemble mean zonal wind stress annual climatology (top) and the difference between observations and ensemble mean precipitation annual climatology (bottom) from fourteen CMIP5 AMIP runs. The length of observational data used in the calculation is 30 years for CMAP precipitation and SODA zonal wind stress (1979–2008). The length of data used for AMIP runs is the same as for Figure 8.

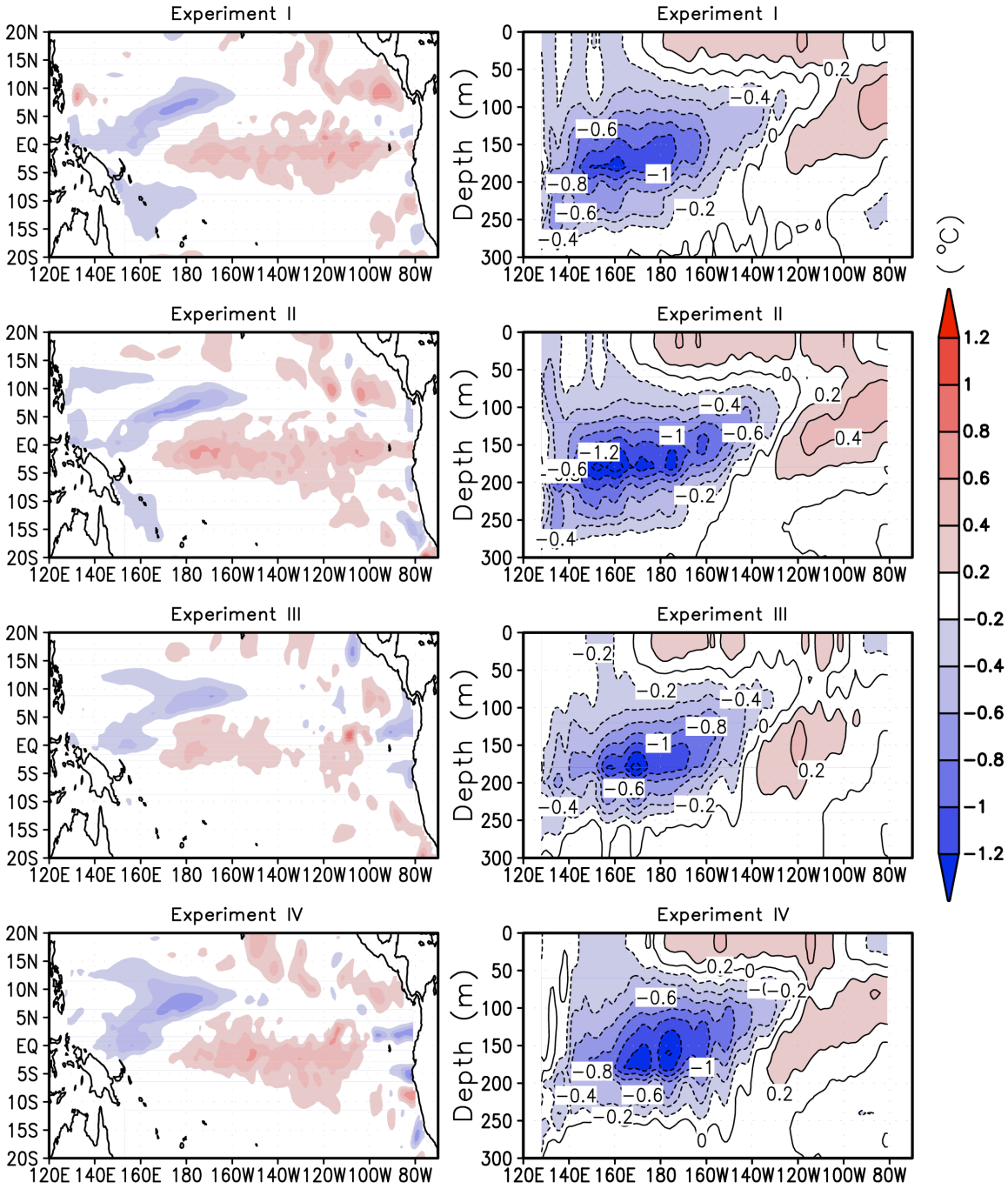


Figure 14: The sum of the composite anomalies of the two phases of ENSO for SST (left panel) and the equatorial (5°S-5°N) upper ocean temperature (right panel) in the four forced ocean experiments as listed in Table 1.

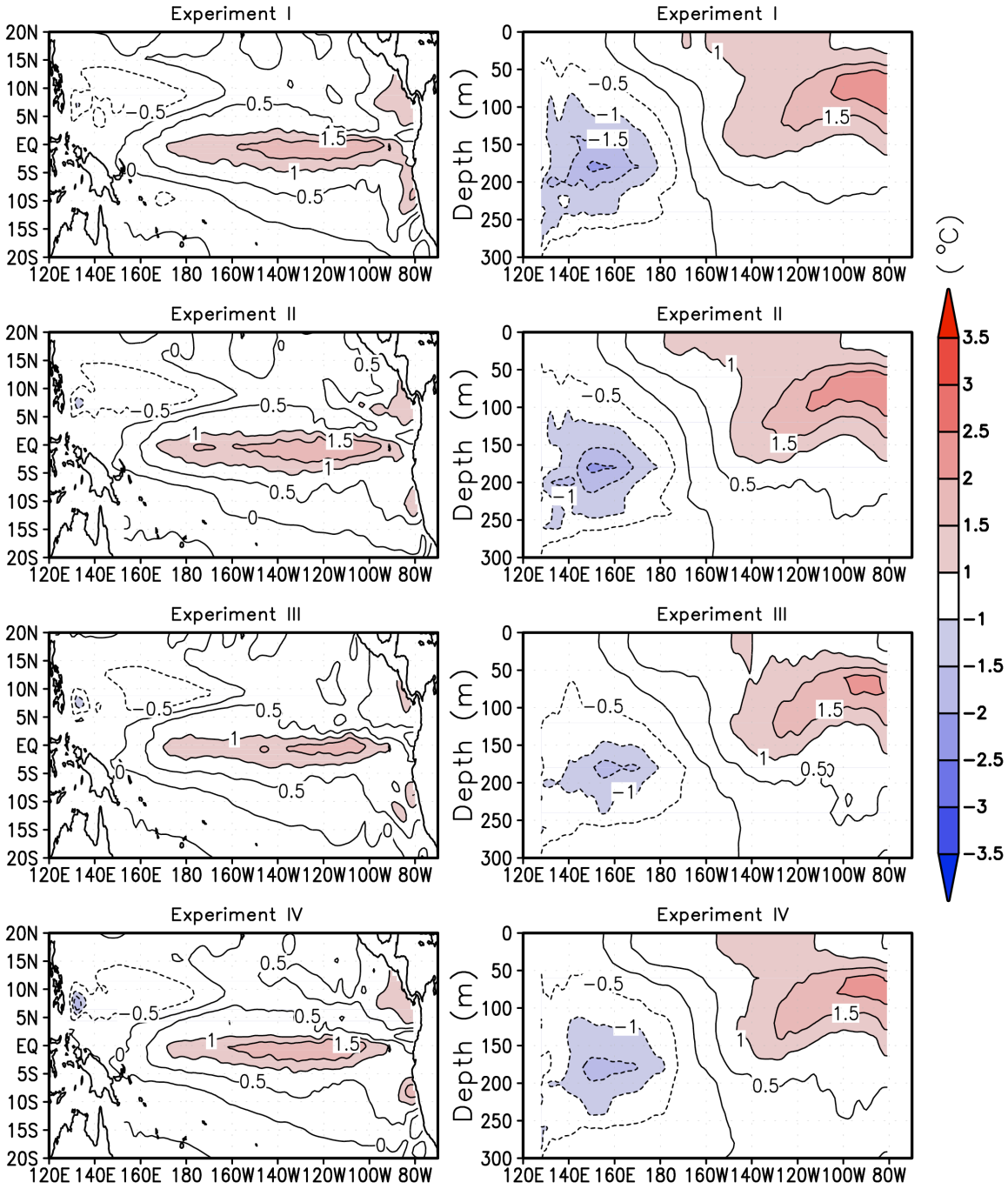


Figure 15: Composite anomalies of SST (left panel) and the equatorial (5°S-5°N) upper ocean temperature (right panel) for the warm phase of ENSO in the four forced ocean experiments as listed in Table 1.

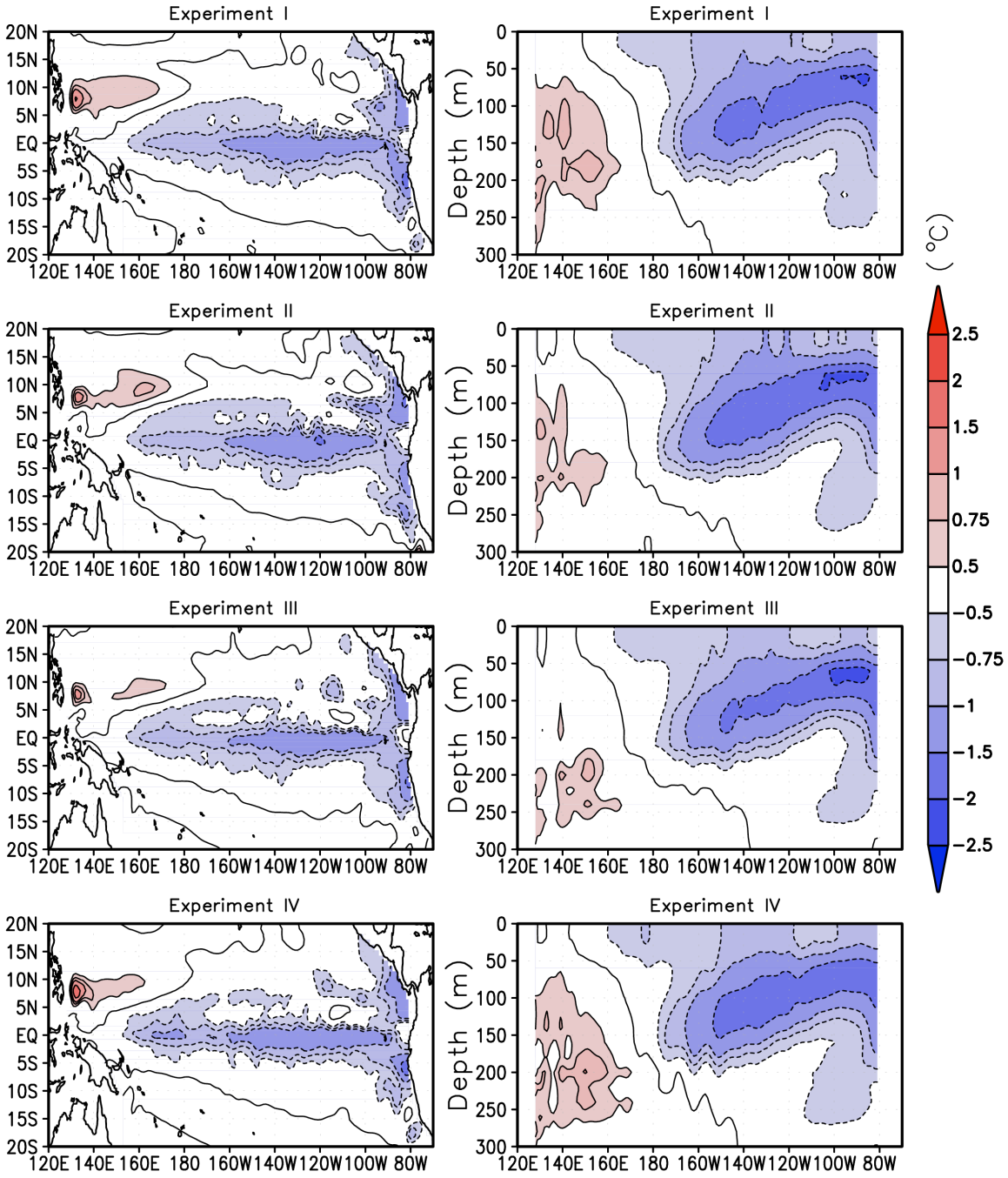


Figure 16: Composite anomalies of SST (left panel) and the equatorial ($5^{o}$S-$5^{o}$N) upper ocean temperature (right panel) for the cold phase of ENSO in the four forced ocean experiments as listed in Table 1.

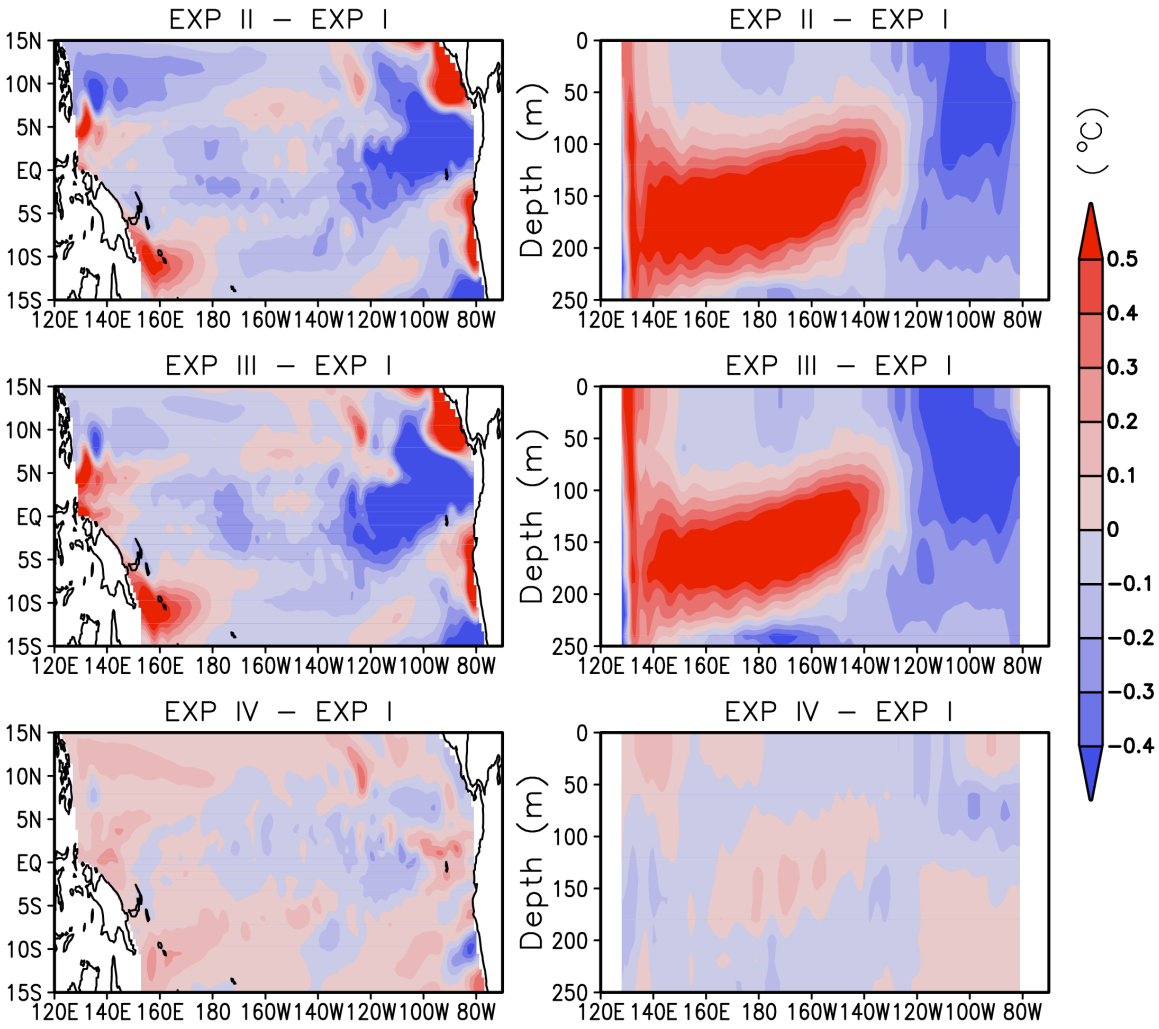


Figure 17: Time mean SST difference (left panel) and the equatorial ($5^{o}$S-$5^{o}$N) upper ocean temperature difference (right panel) of Experiment II, Experiment III, and Experiment IV from Experiment I.